JAERI-M
91-019

PROGRESS REPORT ON SAFETY RESEARCH ON HIGH-LEVEL WASTE MANAGEMENT FOR THE PERIOD APRIL 1989 TO MARCH 1990

February 1991

(Eds.) Susumu MURAOKA, Muneaki SENOO and Yoshii KOBAYASHI

日本原子力研究所
Japan Atomic Energy Research Institute

JAERI-Mレポートは，日本原子力研究所が不定期に公刊している研究報告書です。
入手の問合わせは，日本原子力研究所技術情報部情報資料課（〒319-11茨城県那珂郡東海村）あて，お申しこしください。なお，このほかに財団法人原子力弘済会資料センター（〒319-11 茨城県那珂郡東海村日本原子力研究所内）で複写による実費頒布をおこなっております。

JAERI-M reports are issued irregularly.
Inquiries about availability of the reports should be addressed to Information Division, Department of Technical Information, Japan Atomic Energy Research Institute, Tokai-mura, Naka-gun, Ibaraki-ken 319-11, Japan.

編集兼発行　日本原子力研究所
印　　刷　㈱原子力資料サービス

JAERI-M 91-019

Progress Report on Safety Research on High-Level Waste Management for the Period April 1989 to March 1990

(Eds.) Susumu MURAOKA, Muneaki SENOO and Yoshii KOBAYASHI

Department of Environmental Safety Research
Tokai Research Establishment
Japan Atomic Energy Research Institute
Tokai-mura, Naka-gun, Ibaraki-ken

(Received January 31, 1991)

Research on high-level waste management at the Engineered Barrier Materials Laboratory, Environmental Geochemistry Laboratory and Environmental Radiochemistry Laboratory of the Department of Environmental Safety Research, JAERI in the fiscal year of 1989 are described.

The topics are as follows:

1) As for waste forms and engineered barrier material, performance assessment studies on glass and ceramic forms, and corrosion test of carbon steel were continued.
2) In the safety evaluation study for geological disposal, chemical behavior of nuclide in water, nuclide migration and retardation in geosphere were studied. New microspectrometers was developed to analyze the chemical form in rocks.
3) Distribution and migration of uranium in uranium ore were examined as a natural analogue study.

Keywords: High-Level Radioactive Waste, Waste Forms, Engineered Barrier Material, Glass, Ceramic, Migration, Retardation, Geosphere, Microspectrometers, Uranium, Natural Analogue

JAERI－M 91－019

高レベル廃棄物処理処分の安全性に関する平成元年度報告書

日本原子力研究所東海研究所環境安全研究部
（編）村岡　進・妹尾　宗明・小林　義威

（1991年1月31日受理）

人工バリア研究室，深地処分研究室及び環境放射化学研究室において，平成元年度に実施した高レベル廃棄物処理処分の安全性に関する研究成果を報告書にまとめた。

その内容は次の通りである。

1）固化体及び人工バリア材の研究開発では，ガラス固化体，セラミック固化体の性能評価試験及び容器材料の耐食性試験を継続した。

2）地層処分の安全評価試験では，核種の水中での化学的挙動，地層中での核種の移行・遅延挙動の研究を実施した。また，岩石中の元素の化学形分析法の開発を進めた。

3）ナチュラルアナログ研究として，ウラン鉱床中のウランの分布及び移行に関する研究を実施した。

東海研究所：〒319－11 茨城県那珂郡東海村白方字白根2－4

Contents

目　　次

Introduction

In order to achieve the safe disposal of high-level radioactive waste, it is necessary to promote the development of waste management and safety assessment methodology.

The Japan Atomic Energy Research Institute (JAERI) has conducted safety assessment study and development of new technology to contribute the establishment of national system for the high-level radioactive waste management in Japan.

This report summarizes the status and results of studies performed in the fiscal year 1989 at the Engineered Barrier Materials Laboratory, Environmental Geochemistry Laboratory and Environmental Radiochemistry Laboratory of the Department of Environmental Safety Research, JAERI.

The progress report series have been issued in the following numbers; JAERI-M 82-145, 83-076, 84-133, 85-090, 86-131, 87-131, 88-201 and 89-192.

1. Research and development of waste forms and container materials

1.1 Performance of glass waste forms

1.1.1 Leaching behavior of high-level waste glass in synthetic groundwater

H. Kamizono

The characteristics of groundwater affect leaching behavior of high-level waste glass, for example pH and Eh values may determine the precipitation processes of some elements in water. In the reduced synthetic groundwater which contains carbonate and sulfate ions, simulated high-level waste glass was subjected to static leach tests at 70° ± 1° and 20° ± 5°C. The glass-surface-area to leachant-volume ratio (SA/V ratio) was 0.24 cm^{-1} at 70°C and 0.12 cm^{-1} at 20°C. The static leach test at 70°C for up to 49 days was carried out in order to observe the process quickly. The static leach test at 20°C for 1 year was carried out for comparison with a former in-situ leach tests in one type of Japanese natural groundwater at 14°C. The four kinds of synthetic groundwater listed in Table 1 were used as leachants instead of the natural groundwater. Deionized water with a pH value of 5.6 and a specific resistance of 10^7 ohm·cm was used as a reference.

Among normalized elemental mass losses (NL values) for the six elements, i.e., B, Si, Al, Fe, Nd and Ba, the value of NL_B was highest without exception, and the value of NL_{Ba} was lowest in some cases. The variation of NL_{Fe} is of particular interest, since it tended to be low in the case of deionized water and it was as high as NL_B in the case of synthetic groundwater Nos.1 to 3 at 20°C. The ratio of NL_{Fe}/NL_B is introduced as an index expressing the extent of congruence. Table 2 summarizes the ratios of NL_{Fe}/NL_B under the present experimental conditions. The results in Table 2 can be interpreted in two ways. First, the ratio in synthetic groundwater tends to be higher than that in deionized water for each temperature and time condition, which means that in synthetic groundwater Fe tends to dissolve more congruently and not to precipitate on the glass surface during leaching. Second, when the kind of water is fixed, the ratios of NL_{Fe}/NL_B are ordered as:

(20°C, 1 year) > (70°C, 28 days) > (70°C, 49 days)

with the exception of synthetic groundwater No.4 where a slight variation occurs.

1. Research and development of waste forms and container materials

1.1 Performance of glass waste forms

1.1.1 Leaching behavior of high-level waste glass in synthetic groundwater

H. Kamizono

The characteristics of groundwater affect leaching behavior of high-level waste glass, for example pH and Eh values may determine the precipitation processes of some elements in water. In the reduced synthetic groundwater which contains carbonate and sulfate ions, simulated high-level waste glass was subjected to static leach tests at 70° ± 1° and 20° ± 5°C. The glass-surface-area to leachant-volume ratio (SA/V ratio) was 0.24 cm^{-1} at 70°C and 0.12 cm^{-1} at 20°C. The static leach test at 70°C for up to 49 days was carried out in order to observe the process quickly. The static leach test at 20°C for 1 year was carried out for comparison with a former in-situ leach tests in one type of Japanese natural groundwater at 14°C. The four kinds of synthetic groundwater listed in Table 1 were used as leachants instead of the natural groundwater. Deionized water with a pH value of 5.6 and a specific resistance of 10^7 ohm·cm was used as a reference.

Among normalized elemental mass losses (NL values) for the six elements, i.e., B, Si, Al, Fe, Nd and Ba, the value of NL_B was highest without exception, and the value of NL_{Ba} was lowest in some cases. The variation of NL_{Fe} is of particular interest, since it tended to be low in the case of deionized water and it was as high as NL_B in the case of synthetic groundwater Nos.1 to 3 at 20°C. The ratio of NL_{Fe}/NL_B is introduced as an index expressing the extent of congruence. Table 2 summarizes the ratios of NL_{Fe}/NL_B under the present experimental conditions. The results in Table 2 can be interpreted in two ways. First, the ratio in synthetic groundwater tends to be higher than that in deionized water for each temperature and time condition, which means that in synthetic groundwater Fe tends to dissolve more congruently and not to precipitate on the glass surface during leaching. Second, when the kind of water is fixed, the ratios of NL_{Fe}/NL_B are ordered as:

(20°C, 1 year) > (70°C, 28 days) > (70°C, 49 days)

with the exception of synthetic groundwater No.4 where a slight variation occurs.

Grooves were observed on the surface of the specimens leached in synthetic groundwater Nos.1 to 4. However, they were not clearly observed on the specimen leached in deionized water. It is thought that the grooves are clear in synthetic groundwater Nos.1 to 4 when congruent leaching tends to occur and not clear in deionized water when incongruent leaching occurs. Such grooves were also observed on the surface of the specimens leached in natural groundwater.

In synthetic groundwater Nos.1 to 4 which are reduced by tris-(hydroxymethyl)-aminomethane (THAM), the amount of Fe in the leachates increases as the Si increases probably as a result of the formation of $FeSiO_3$ colloidal particles or $FeSi_3O_3(OH)_8$ complex. It is not true that Fe very quickly reaches its saturation limit in synthetic groundwater Nos.1 to 4, since the formation of the colloids or complex will increase the solubility of Fe in leachates. Because the filtration of the leachate at 20°C for 1 year through a 0.025 μm membrane had almost no effect on the concentrations of Fe and Si, $FeSiO_3$ colloidal particles, if present, have a diameter of less than 0.025 μm.

In deionized water in an oxidized condition, NL_{Fe}/NL_B was smaller than that of synthetic groundwater, but this is not because of the higher pH values of the leachates. For example, in deionized water at 20°C the pH value was 7.3 and smaller than that in synthetic groundwater. Even in deionized water, there is at least one example in which the solution concentration of Fe does not decrease as the pH value increases. This example was observed with leach experiments at a high SA/V ratio of 0.85 cm^{-1}.

The role of THAM should be mentioned here. It tends to increase the pH and to decrease the Eh of the solution. The pH values of the present synthetic groundwater were adjusted to 7.7 (Table 1), and for this purpose about 5 g of THAM were used for a 1 liter solution. The use of THAM is though to be a major cause for the congruent dissolution of the glass in synthetic groundwater Nos.1 to 4, since an Eh decrease by THAM in leachants will work effectively to form $FeSiO_3$ colloids or $FeSi_3O_3(OH)_8$ complex. As temperature rises and as time proceeds, THAM as a reducing agent will be consumed with the progress of leaching, resulting in a lower NL_{Fe}/NL_B ratio.

In conclusion, the examination of the leaching behavior of high-level waste glass in synthetic groundwater is quite useful for

identifying and understanding the mechanisms involved. Under somewhat reducing conditions, Fe dissolves easily into leachates, and hydrated silicate surface layer on the glass surface tends to dissolve more easily with Fe in reduced synthetic groundwater that in deionized water. In synthetic groundwater, cracks originally present on the glass tend to open and are observed as evidence of congruent glass corrosion. It is speculated that, in deep geologic disposal sites, congruent dissolution is more likely to occur in a reducing environemnt with a high SA/V-ratio.

References

1) H. Kamizono, "Congruent Dissolution of High-Level Waste Glass in Synthetic Groundwater," J. Nucl. Mater., 172, 319-324 (1990).

2) H. Kamizono, "Effects of Carbonate and Sulphate Ions in Synthetic Groundwater on High-Level Waste Glass Leaching," J. Mater. Sci. Lett., 9, 841-844 (1990).

Table 1 Composition of synthetic groundwater.

	Synthetic groundwater			
	No.1	No.2	No.3	No.4
pH	7.7	7.7	7.7	7.7
Na (in mg/L)*	26	26	26	26
Ca	120	120	-	-
Mg	108	108	108	-
HCO_3^-	Nearly saturated			
SO_4^{2-}	380	-	-	-

- : Not included.

*The amount of each element in the synthetic groundwater is in the average concentration range of the respective element in the natural groundwater.

Table 2 The ratio of NL_{Fe}/NL_B in the leachates.

Leach conditions	Synthetic groundwater				Deionized water
	No.1	No.2	No.3	No.4	
70°C, 28 days	0.35	0.36	0.66	0.24	0.0021
70°C, 49 days	0.13	0.24	0.20	0.51	0.0014
20°C, 1 year, (Not filtered)	0.85	0.98	0.97	0.55	0.14
20°C, 1 year, (Filtered)	1.02	0.82	1.01	0.59	0.16

1.1.2 Density phenomena of an actinide-doped borosilicate waste glass

T. Banba and Y. Inagaki

The effects of annealing treatment on the density of an self-irradiated borosilicate waste glass were studied in the temperature range from 200°C to 500°C. The bulk composition of an actinide-doped glass sample is shown in Table 1. The glass sample used for the experiment had a cumulative dose of 1.7×10^{19} alpha decays/cm^3. The densities of the glass specimens were measured by a sink-float method using two kinds of organic mixtures composed of 1-1-2-2-tetra-bromoethane and alpha-bromonaphtalene.

In isochronal annealing increases in density were observed at annealing temperatures below 450°C. Conversely, above that temperature the density decreased as shown in Fig. 1. This seems to be the reason that the annealing temperature approached the transition range of the waste glass. The density in isothermal annealing increased rapidly in the initial 5 hours and approached to its equilibrium value at each temperature. As an example, the density change in isothermal annealing for irradiated specimens at 450°C is shown in Fig. 2.

The implications of these results were discussed using the model on the basis of the formation of helium bubbles in the glass and the recovery of network distortion. The density change of the post-irradiation annealing glass by the formation of helium bubbles is represented by the following equation.

$$\rho_{tr}(t) = \frac{\rho_0}{1+(4/3)\pi R(t)^3 N} \qquad (1)$$

where $\rho_{tr}(t)$ is the density of the glass sample at the annealing time t, ρ_0 is the density of the unirradiated glass sample, R(t) is the radius of helium bubbles, and N is the number of helium bubbles per unit volume of glass sample. R(t) can be calculated by using the N, the surface tension of the glass: γ, and the number of He atoms in a bubble: m(t), which have been already obtained by other experimental works[1),(2),(3)]. On the other hand, the density change by the recovery of glass network distortion is estimated by the following equation.

$$\rho_{dis}(t) = \left[1 + \left(\frac{\rho(\infty)}{\rho_b} - 1 \right) \{ 1 - \exp(-Bt) \} \right] \rho_b \qquad (2)$$

where $\rho_{dis}(t)$ is the density of the glass sample at the annealing time t, $\rho(\infty)$ is the density of the glass sample at $t = \infty$, ρ_b is the density of the glass sample at $t = 0$, and B is the constant on the distortion recovery. Figure 3 shows the curves of density change calculated by the equation (1) (trapping model), by the equation (2) (distortion model), and by the summation of equation (1) and (2) (total) under the isothermal annealing at 450°C. As seen from this figure the experimental data agree well with the values calculated by the model including both the formation of helium bubbles in the glass and the recovery of network distortion.

References

1) H. Furuya et al., Proc. the first meeting on the JAERI/Universities co-operative program, p87 (1990).
2) S. Sato et al., J. Nucl. Mater., **152**, 265 (1988).
3) J.F. DeNatale and D.G. Howitt, Nucl. Instr. and Meth., **B1**, 489 (1984).

Table 1 Bulk composition of an actinide-doped borosilicate waste glass.

Component	wt %	Component	wt %
Additives		Wastes	
SiO_2	45.15	Cs_2O	0.97
B_2O_3	13.90	BaO	0.62
Al_2O_3	4.89	La_2O_3	0.14
Li_2O	2.00	CeO_2	0.28
Na_2O	9.78[a]	Pr_6O_{11}	0.14
CaO	4.00	Nd_2O_3	0.45
ZnO	2.47	Sm_2O_3	0.09
		Eu_2O_3	0.02
Wastes		Gd_2O_3	0.01
Rb_2O	0.12	SeO_2	0.02
SrO	0.34	RuO_2	0.80
Y_2O_3	0.06	Fe_2O_3	2.90
ZrO_2	2.64[b]	NiO	0.40
MoO_3	1.73	Cr_2O_3	0.50
MnO_2	0.26	P_2O_5	0.30
Ag_2O	0.03	Ru	0.12
CdO	0.03	Rh	0.15
SnO_2	0.02	Pd	0.43
Sb_2O_3	0.01	Cm Oxides[c]	3.04
TeO_2	0.23	Pu Oxides[d]	0.96
		Total	100.00

[a] Partly contains Na_2O as chemicals added in the reprocessing.
[b] Partly contains ZrO_2 as zircalloy filings.
[c] See Table 2 which shows the radionuclide content of curium source.
[d] See Table 3 which shows the radionuclide content of plutonium source.

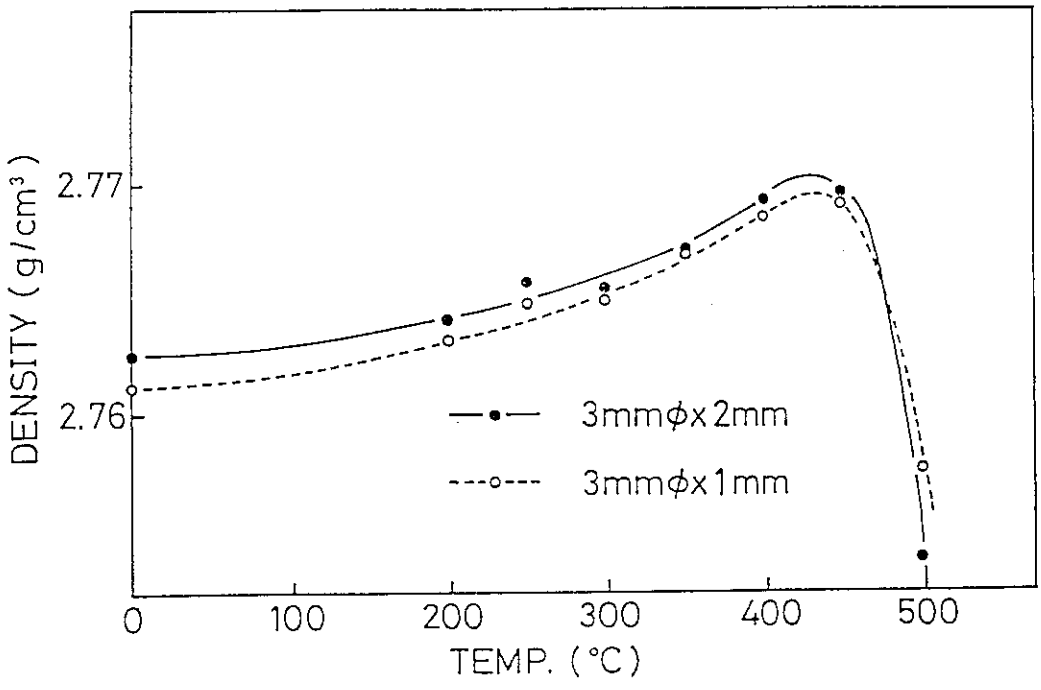

Fig. 1 Density change in isochronal annealing for 1 hour at each temperature for irradiated specimens.

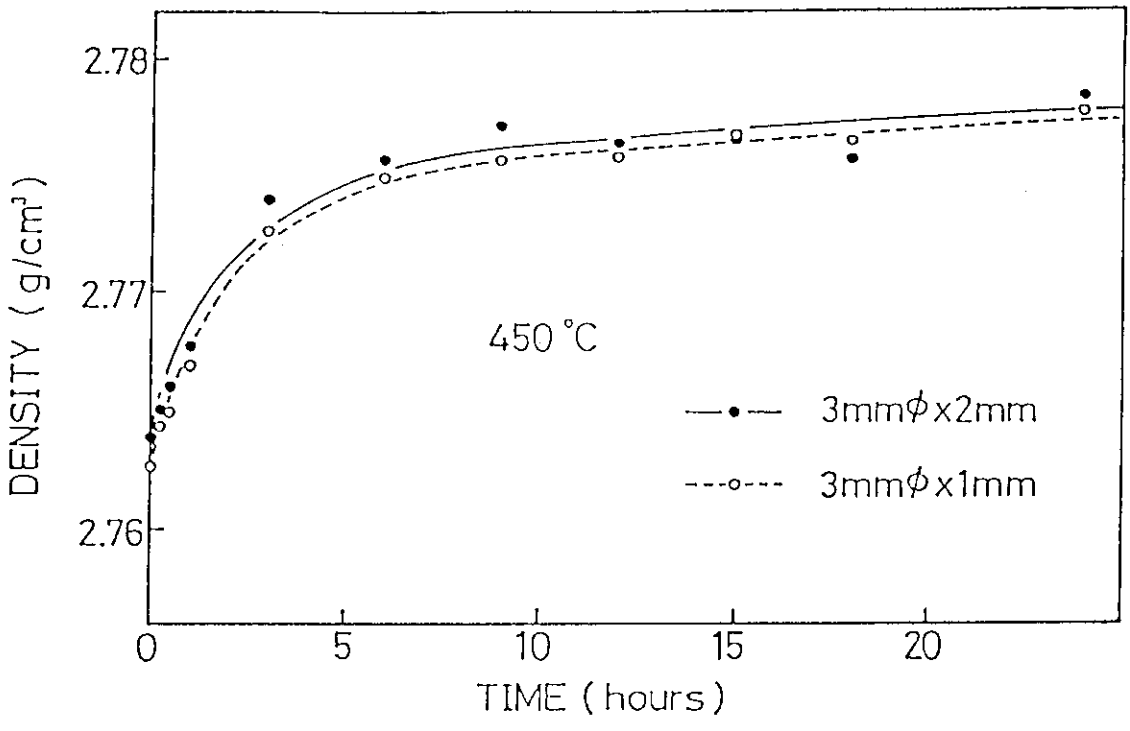

Fig. 2 Density change in isothermal annealing for irradiated specimens at 450°C.

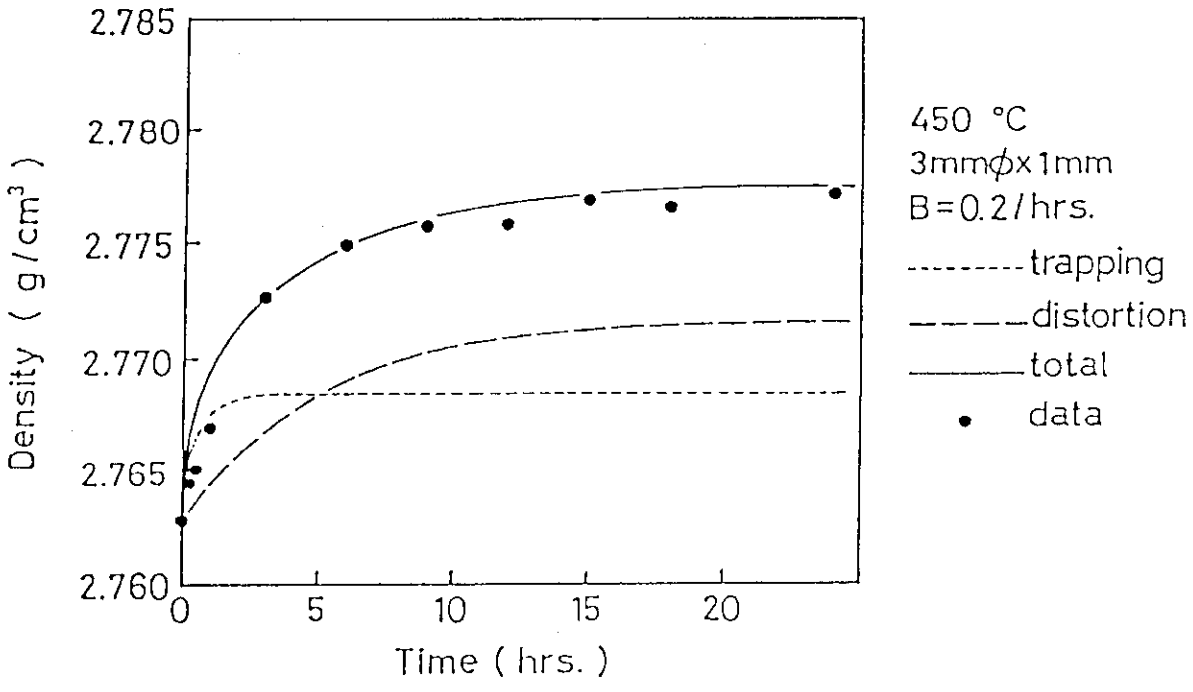

Fig. 3 The curves of density change calculated by the models based on the formation of helium bubbles in the glass (trapping model) and on the recovery of glass network distortion (distortion model) in isothermal annealing at 450°C. Solid circles show the experimental data.

1.2 Performance of ceramic waste forms

1.2.1 Chemical durability of Synroc in accelerated self-irradiation test

H. Mitamura, S. Matsumoto, Y. Togashi,
T. Sagawa, Y. Tamura

Introduction

The Synroc phase assemblage has considerable flexibility to respond to expected variations in waste stream compositions which arise from reprocessing nuclear fuel [1]. Existing Japanese HLW contains high concentrations of processing contaminats such as sodium and iron, which promote formation of less durable sodium-rich phases [2]. As HLW contains long-lived actinide elements, Synroc will suffer long-term self-irradiation due to alpha decays. This self-irradiation can deleteriously affect stability of the waste form by, for example, inducing anisotropic dimensional changes that lead to cracking and an increase in the surface area exposed to ground water. In this case, the less durable phases are no longer encapsulated in the resistant matrix and are more easily accessed by ground water. In the present paper, curium-doped Synroc was leach tested to study the effects of alpha-decay damage on chemical durability of Synroc incorporating sodium-rich simulated HLW.

Experimental

Curium-doped Synroc was hot-pressed at 1200°C and 29 MPa for 2 h in a hot cell [3]. The ^{244}Cm content and specific ^{244}Cm activity were 0.69 wt% and 20.6 $GBq \cdot g^{-1}$, respectively, on November 1, 1987 [3]. The rims of 2-cm dia × 1-cm high blocks were polished with #600 grit abrasive paper. Some of the block samples each were slit horizontally into five discs. These discs were cut across their diameters after their flat faces were lapped with 6-micron diamond paste. The cut surface of each half-disc was also finished with 6-micron diamond paste.

Curium-doped half-disc specimens, which had accumulated different levels of alpha-decay damage up to an equivalent age of 11000 years, were leach tested by MCC-1 method at 90°C in pure water. The size of half-disc specimens was 2-cm dia × ca 0.1-cm thick. The specimen surface area to leachant volume ratio was 10 m^{-1}. The leach container

was charged with leachant, a sample support, and a half-disk specimen. Every seven days for the first month, this half-disc specimen was transferred into fresh leachant in a new leach container with a new sample support, and then a further 28-day leaching run was performed. Each run consisted of a set of three specimen-charged leach containers and a specimen-free reference container.

After pH measurement, the leachate samples were taken out of the glove box. Radioactive contamination on each leach container was checked by the smear method, and the amount of ^{244}Cm leached was measured using well-type NaI(Tl) gamma-ray spectrometry [4]. After concentration of leachate, nonradioactive elements were analyzed by atomic absorption spectrometry and inductively coupled plasma spectroscopy.

Results and discussion

In leaching runs on 130- and 330-year Synroc, the average pH of three specimen-charged samples varied in concert with the specimen-free leachate, although the pH of the specimen-charged samples was always lower [5]. In leaching runs on 11000-year Synroc, the average pH of three specimen-charged samples is always higher than that of specimen-free leachate, and this pH reaches 8.4 after the final 28-day leach period (Fig. 1).

Concerning leach rates of non-radioactive elements from 130- and 330-year Synroc, their leach rates tended to decrease abruptly after the initial seven-day leach period and approached their constant values at longer times [5]. This phenomenon is observed in good quality Synroc. In leaching runs on 2000-year Synroc, one of the three specimens exhibited very erratic behavior [5]. The difference between specimens is probably caused by different degrees of crack propagation which results in exposure of fresh surfaces to the leachant. The leach rates of the non-radioactive elements from 11000-year samples (Fig. 2) are higher than the younger samples by more than one order of magnitude. The fluctuation of leach rates for alkali metals with time suggests that grain boundary glassy phases controlled their leach rates from the Synroc specimens. This shows that microencapsulation effect of the resistant matrix of Synroc is significantly deteriorated possibly due to crack propagation induced by volume swelling.

Although the difference amongst the three data sets was large, curium leach rates up to an equivalent age of 2000 years appeared to gradually increase with Synroc age [5]. On the other hand, curium release from 11000-year Synroc (Fig. 3) is lower than younger Synroc by more than one order of magnitude. This reduction is possibly due to high pH of leachates. The damage effects on the chemical durability must be further clarified by work which is continuing for longer Synroc ages.

References

1) A.E. Ringwood and P.M. Kelly, "Immobilization of High-Level Waste in Ceramic Waste Forms," Phil. Trans. R. Soc. Lond. A., 319, 63-82 (1986).

2) W.J. Buykx, K. Hawkins, D.M. Levins, H. Mitamura, R. St. C. Smart, G.T. Stevens, K.G. Watson, D. Weedon, and T.J. White, "Titanate Ceramics for the Immobilization of Sodium-Bearing High-Level Nuclear Waste," J. Am. Ceram. Soc., 71[8], 678-688 (1988).

3) H. Mitamura, S. Matsumoto, W.J. Buykx, and S. Tashiro, "Fabrication of Curium-Doped Synroc for an Alpha Radiation Stability Test," Nucl. Technol., 85, 109-117 (1989).

4) H. Mitamura, Y. Togashi, S. Matsumoto, T. Miyazaki, Y. Tamura, and S. Tashiro, "Well-Type NaI(Tl) Spectrometry for Quantitative Analysis of ^{244}Cm Leached from Curium-Doped Synroc," Int. J. Radiat. Appl. & Instr. Part A, 41[9], 839-845(1990).

5) H. Mitamura, S. Matsumoto, T. Miyazaki, T.J. White, K. Nukaga, Y. Togashi, T. Sagawa, S. Tashiro, D.M. Levins, and A. Kikuchi, "Self-irradiation Damage of a Curium-Doped Titanate Ceramic Containing Sodium-Rich High-Level Nuclear Waste," J. Am. Ceram. Soc., 73[11], 3433-3441(1990).

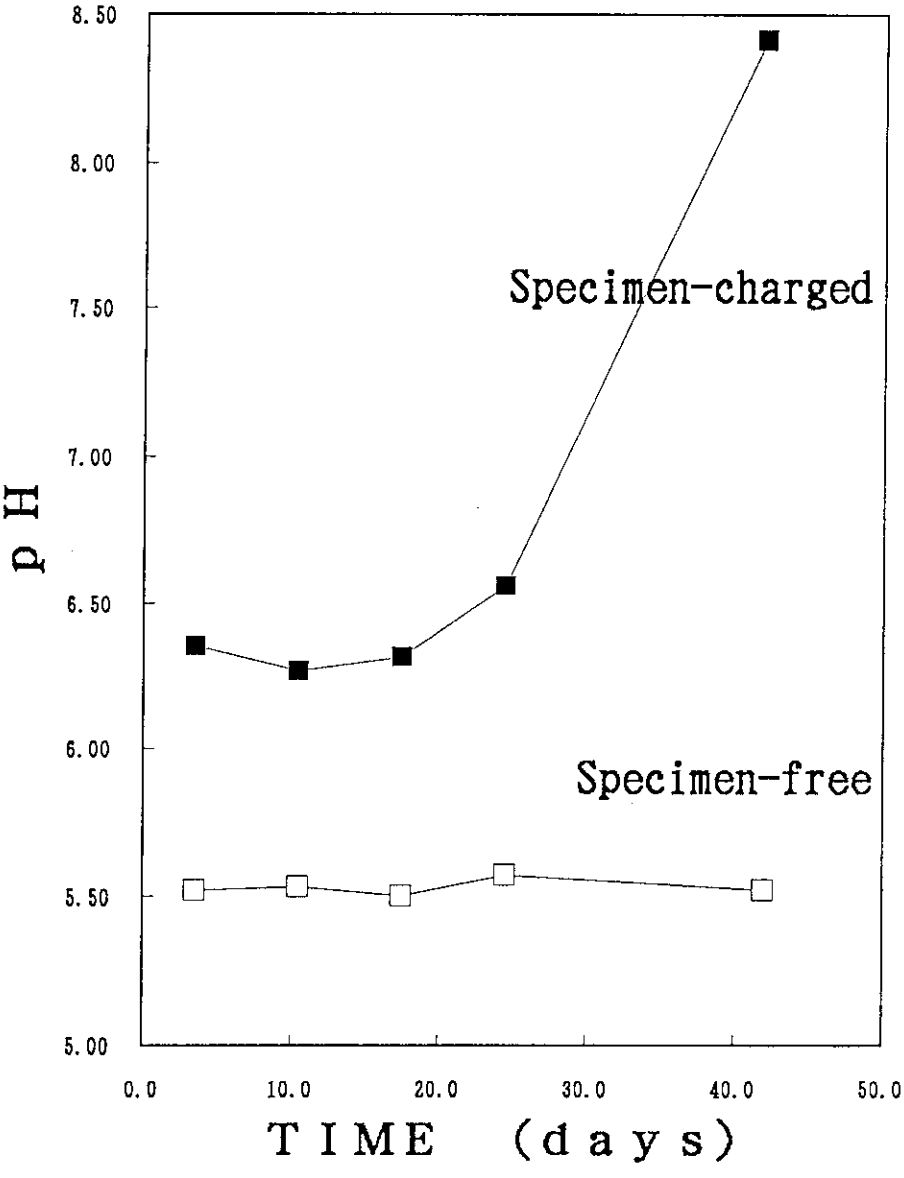

Fig. 1 pH of leachate from 11000-year Synroc specimens versus leach time.

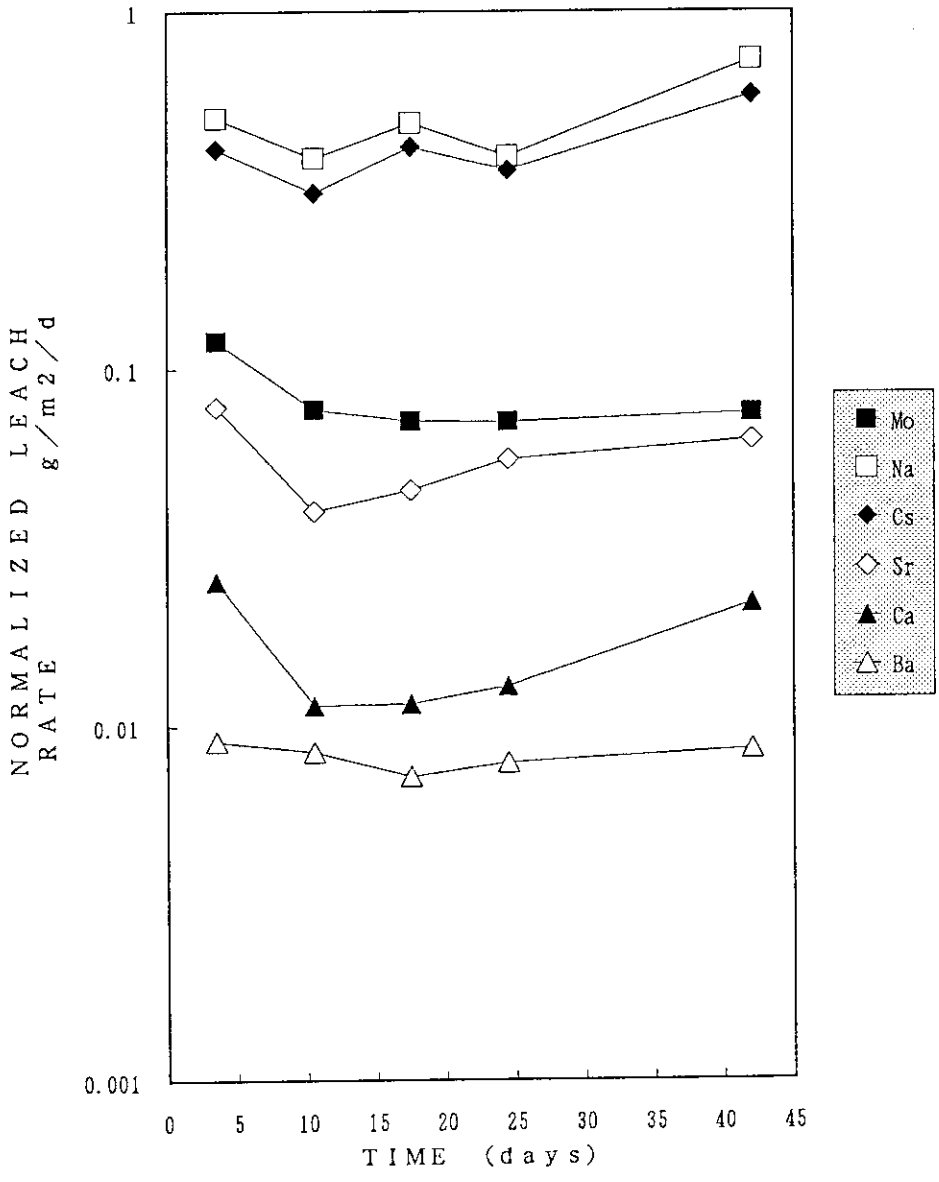

Fig. 2 Normalized leach rates of nonradioactive elements from 11000-year Synroc specimens versus leach time.

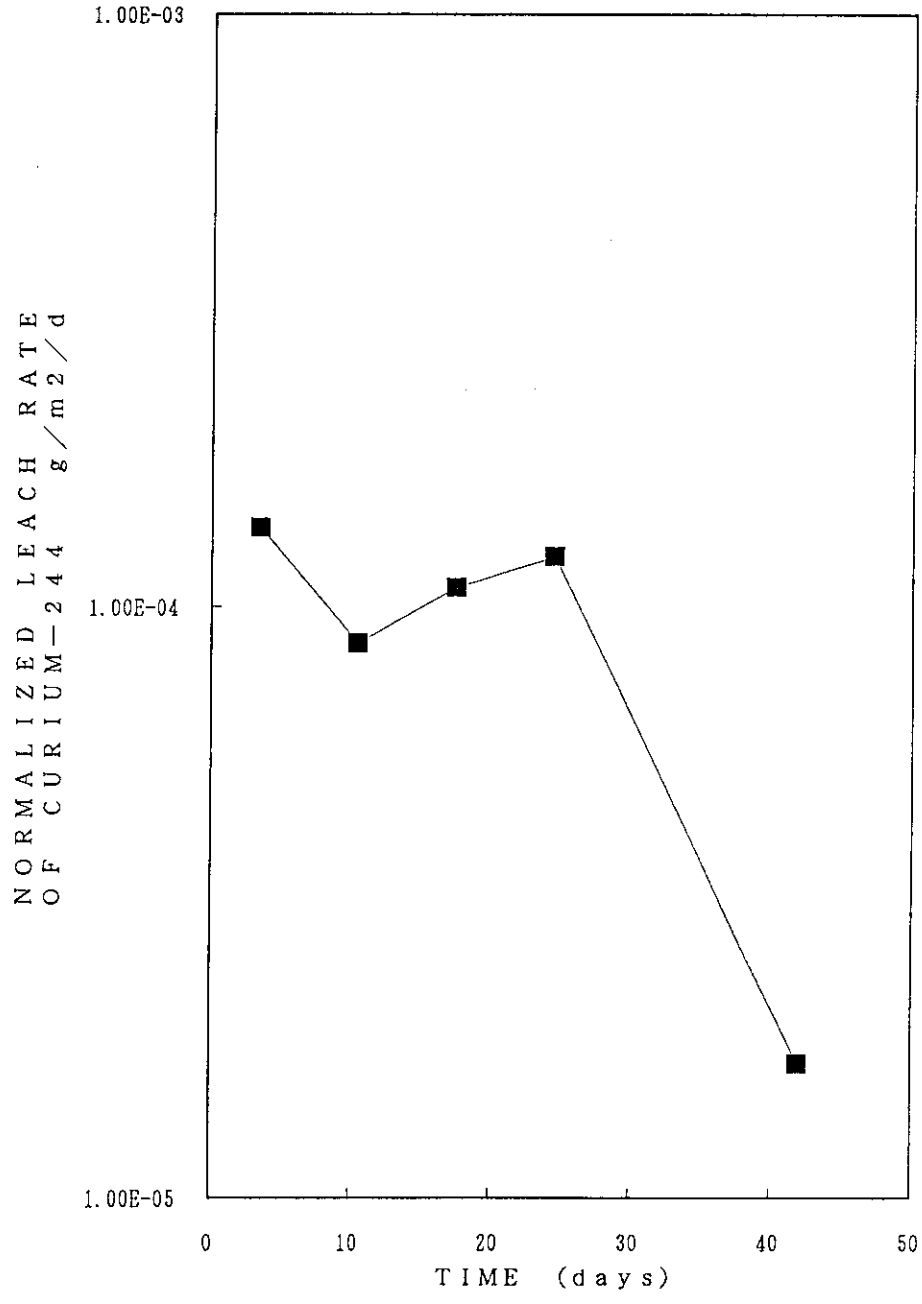

Fig. 3 Normalized leach rate of curium-244 from 11000-year Synroc specimens versus leach time.

1.2.2 Leaching behavior of zirconia-based ceramic waste forms

I. Hayakawa and H. Kamizono

Zirconia-based ceramics may be suitable as host phases which are able to contain hazardous radioactive actinide and lantanide elements in their crystal structures. The durability of four kinds of zirconia-based materials was examined in acid water and in deionized water. The four materials studied are 10 mol% Y_2O_3-stabilized zirconia with a fluorite structure(A), $La_2Zr_2O_7$ with a pyrochlore structure(B), $CaZrO_3$ with a perovskite structure(C) and $ZrTiO_4$(D). The results obtained show that the leach rate of $La_2Zr_2O_7$(B) at 150°C is lowest among four materials, A∿D.

Experimental

The nitrates of the constituents of a host phase were mixed with the nitrates of Ce, Nd and Sr. The quantity of Ce, Nd and Sr added to each host phase corresponds to that of radioactive actinide, lantanide and alkaline earth metal elements contained in 10 wt% HLW. These nitrates were dissolved in water and calcined at 700°C or 800°C. The calcined powder was pressed into pellets and fired at 1400°C for 16 hours in air. The sintered body was crashed to powder. Each powder (A∿D) was identified as a single phase by the X-ray diffractometry. Each crashed powder was leached in acid water(pH=1) at 90°C and in deionized water(pH=5.6) at 90°C and 150°C. After leached for a fixed period, the leached powder was retrieved on a membrane filter and again used for a subsequent leach experiment. The leach rate of each constituent, Li, was calculated as follows:

$$Li = Mi/fi \cdot S \cdot T \ , \qquad (1)$$

where Mi is the mass of constituent i in the leachate, fi is the weight fraction of constituent i in the sample, S is the surface area of the powder and T is the leach time.

Results and discussion

1) Leach rates of the host phase constituents at 90°C

Figure 1 shows the leach rate of the host phase constituents in acid water and in deionized water after 30 days. In acid water, the

leach rate of the host phase constituents decreases in the order of C>D>B>A. The leach rate in deionized water is one or two orders lower than that in acid water and much difference is not observed in the leach rates among A, B and C except for Ca.

It has been reported that Zr stably exists as Zr^{4+} in pH<1.7 and as $Zr(OH)_4$ in pH>1.7[1]. The reactivity between acid water and the material surface determines the concentration of Zr^{4+} in the acid water(pH=1). So it is thought that the leach rate of Zr in acid water depends on the crystalline structure and the Zr-O bond strength of the host phase. However, in deionized water the leach rate of Zr depends on the formation of insoluble $Zr(OH)_4$.

In Fig. 1, Ca shows a high leach rate both in acid water and in deionized water. It is because Ca easily dissolves due to its basic property and does not form insolble materials in both kinds of water.

2) Leach rates of Nd, Ce and Sr at 90°C

Figure 2 shows the leach rates of Nd, Ce and Sr in the acid water and in deionized water after 30 days. In the acid water, the leach rates of these constituents decrease in the order of C>D>>B∿A. The leach rates of Nd and Ce in C, however, decrease by two orders of magnitude in deionized water compared with those in the acid water. The leach rate of Sr in C is high, as is Ca in C. This is because the formation of the solid solution containing Sr during sitering has not been completed.

3) Leach rates of various elements in B at 150°C in deionized water

The leach rate of B at 150°C was lowest among A, B and C. Figure 3 shows that the leach rate of any constituent in B is less that 10^{-4} g/m^2·d after 30 days. This value is lower than that of HLW glass at least by three orders of magnitude. The host phase B can be used for the immobilization of some elements in HLW.

References

1) Brookins, D.G., "Eh-pH Diagrams for Geochemistry", Spring-Verlag Berlin Heiderberg, 1988, pp.116-117.

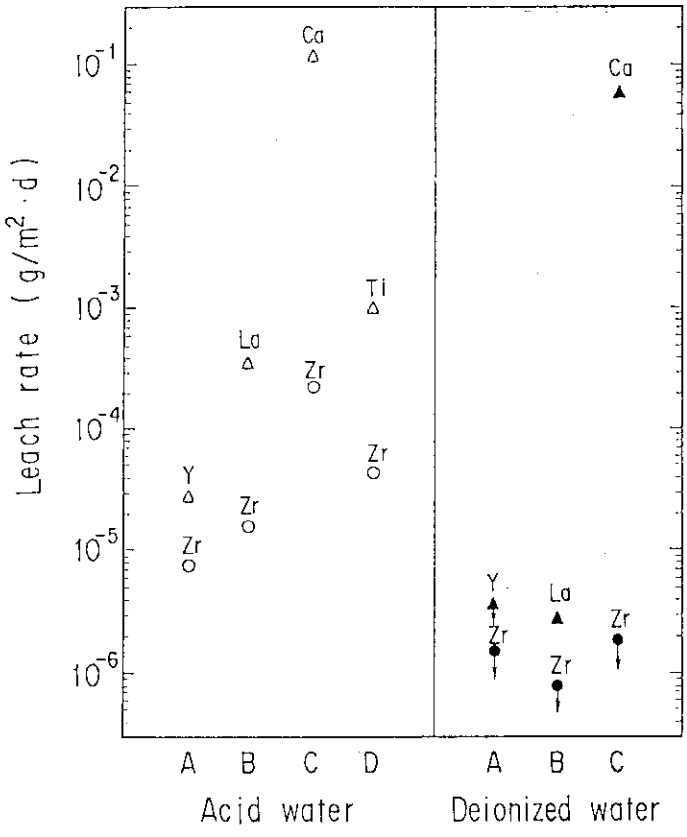

Fig. 1 Leach rates of the host phase constituents in acid water and in deonized water at 90°C after 30 days.

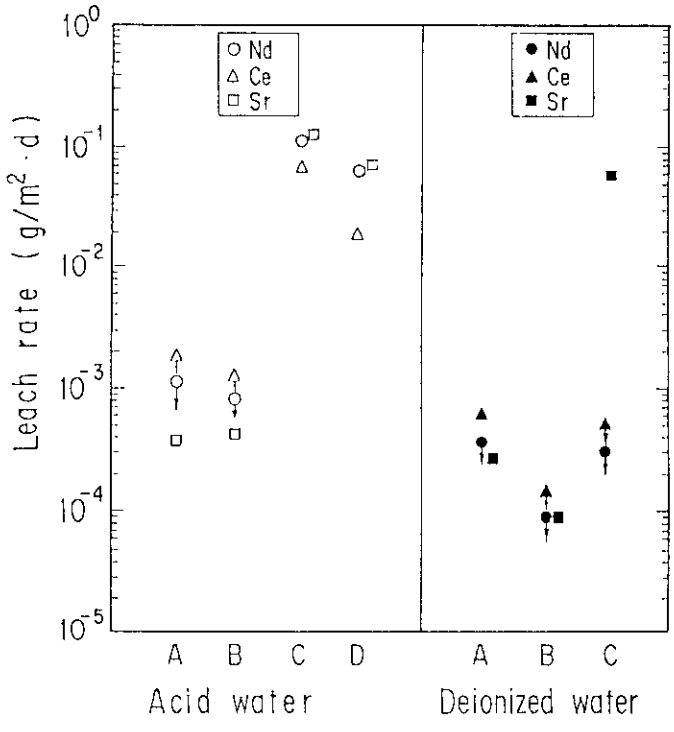

Fig. 2 Leach rates of Nd, Ce and Sr in acid water and in deionized water at 90°C after 30 days.

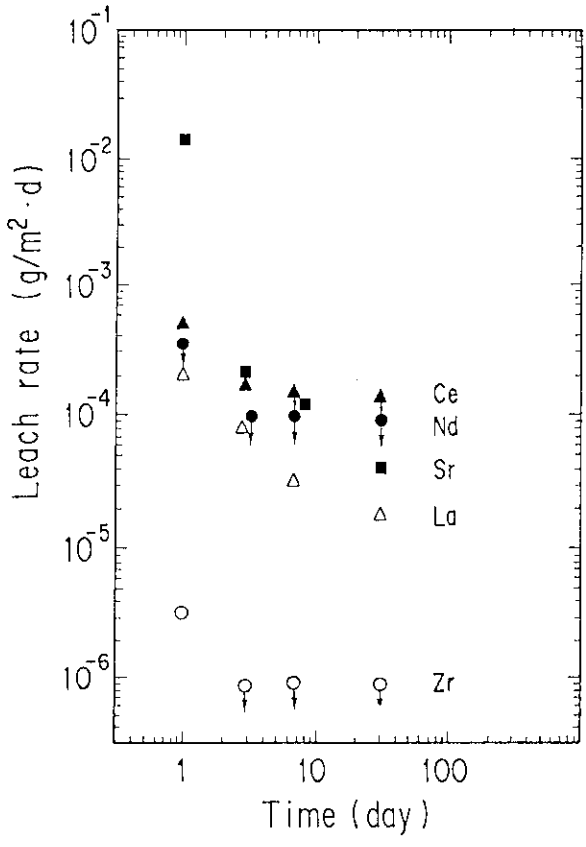

Fig. 3 Leach rate of B in deionized water at 150°C.

1.3 Corrosion of carbon steel in wet bentonite

1.3.1 Evaluation of corrosion rates for carbon steel in wet bentonite

K. Osada and S. Muraoka

Introduction

It is important to evaluate corrosion behavior of carbon steel since it will be used as high level waste containers in a geologic repository. Corrosion tests have been carried out on SS41 carbon steel at 40, 75 and 95°C in wet bentonite, which will be a buffer material around waste containers.

Experimental

Corrosion tests for SS41 carbon steel have been carried out in wet bentonite, and in pure water. One part of bentonite is mixed with five parts of pure water. The specimens of 20mm × 10mm × 3mm in size were placed in a Teflon vessel in a thermostated over at 40, 75 and 95°C. The composition of SS41 carbon steel is shown in Table 1. The composition of bentonite is shown in Table 2. The weights of corroded specimens were measured after the removal of rusts by acetone. Corrosion rates in mm/y were calculated from the weight loss, density and total surface area of the specimens.

Results and Discussion

The results of corrosion rates are shown in Fig. 1. The average corrosion rates were determined by the total weight loss of one year samples, as shown in Table 3. At 40°C, the average corrosion rate of SS41 carbon steel in wet bentonite was 0.03 mm/y. This is smaller than the value of 0.04 mm/y obtained in pure water at 40°C. However, at 95°C, the corrosion rate of SS41 carbon steel in wet bentonite was 0.27 mm/y, which is much larger than that in pure water at 95°C. This is because this specimen in wet bentonite at 95°C was partly covered with bentonite. The corrosion rate of the specimen uniformly covered with bentonite at 95°C was 0.08 mm/y as an example. The corrosion rates were higher at specimens partly covered with bentonite than those uniformly covered with bentonite. In wet bentonite at 95°C, evaporation of moisture resulted in the formation of partial covering of bentonite, which promoted corrosion.

Table 1 Chemical composition of SS41 carbon steel.

	C	Si	Mn	P	S	Cu	Ni	Cr	Fe
%	0.02	0.25	0.40	0.016	0.017	0.13	0.05	0.08	Bal

Bal : Balance

Table 2 Chemical composition of bentonite.

Component	Content(wt%)
SiO_2	65 ～ 75
Al_2O_3	14 ～ 17
Fe_2O_3	1.9 ～ 2.4
CaO	1.2 ～ 1.9
MgO	1.8 ～ 3.0
Na_2O	1.8 ～ 2.5
K_2O	0.5 ～ 1.0
Ig－loss	4.5 ～ 5.0

Table 3 The average corrosion rates (mm/y) of SS41 carbon steel after one year.

	wet bentonite	pure water
95 ℃	0.27	0.08
75 ℃	0.08	0.12
40 ℃	0.03	0.04

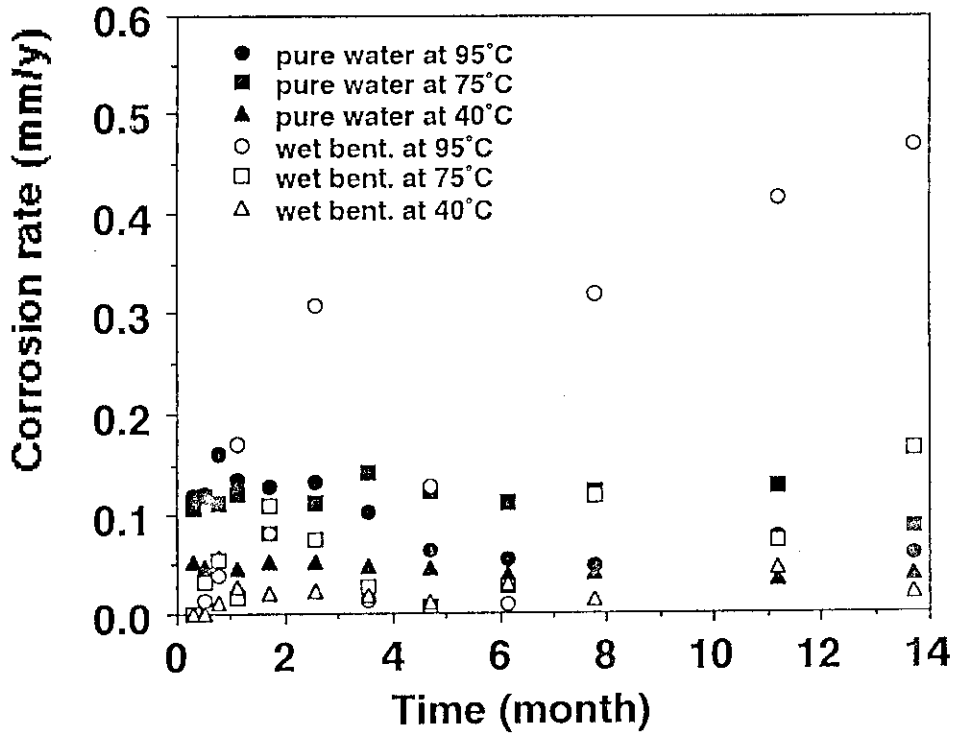

Fig. 1 Corrosion rates of SS41 cabon steel.

1.3.2 Analysis of corrosion products of carbon steel in wet bentonite

K. Osada, T. Nagano and S. Muraoka

Introduction

In order to study corrosion mechanisms of waste container in repository conditions, corrosion products of SS41 carbon steel in wet bentonite have been analyzed by Fourier transform infrared spectroscopy (FT-IR). This method is very useful for characterizing various crystalline and amorphous iron hydroxides.

Experimental

Corrosion products of SS41 carbon steel have been analyzed by FT-IR. The experimental conditions were the same as those in chapter 1.3.1: Specimens have been placed in wet bentonite, and in pure water at 40, 75 and 95°C.

Results and Discussion

Corrosion products in pure water were analyzed by FT-IR and some typical infrared spectra are shown in Fig. 1 and Fig. 2. The peaks of corrosion products in pure water are shown in Fig. 1, those in wet bentonite are shown in Fig. 2. The peaks are attributed to α-FeO(OH) at 880 and 800 cm^{-1} and γ-FeO(OH) at 1020 cm^{-1}. Corrosion product α-FeO(OH) (goethite) was found for all of the experiments conducted in wet bentonite and pure water at 40, 75 and 95°C. Corrosion product γ-FeO(OH) (lepidocrocite) formed at 40°C for all systems. At 75 and 95°C, γ-FeO(OH) formed only in wet bentonite, and it was absent in pure water. This is because water at 75 and 95°C contains less dissolved oxygen, and γ-FeO(OH) could not be formed. In fact, if a cap of experimental vessel is left open, even in pure water at 75 and 95°C, γ-FeO(OH) forms due to evaporation of water. When the partly corroded portions of specimens in wet bentonite at 95°C were sampled, powdered and analyzed in more detail, as shown in Fig. 3. Corrosion product γ-FeO(OH), α-FeO(OH) and $FeSO_4$ were found. Corrosion product γ-FeO(OH) is considered to be formed due to evaporation of moisture, which causes the drying of the metal surface. Corrosion product $FeSO_4$ may be a transitional product transforming into α-FeO(OH).

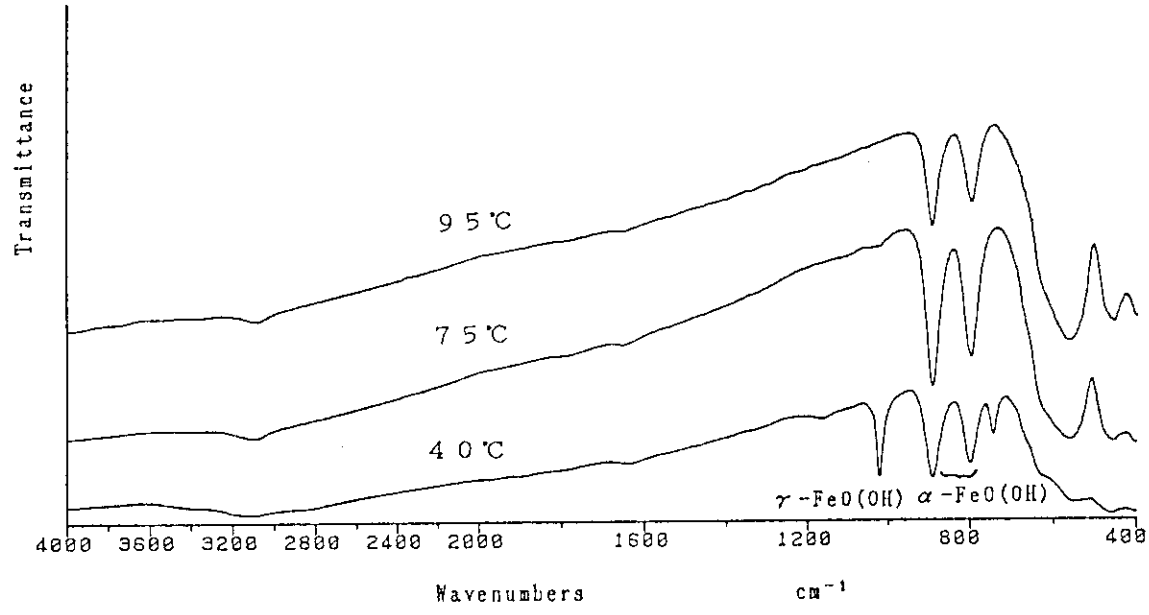

Fig. 1 Analysis of corrosion products in pure water by FT-IR.

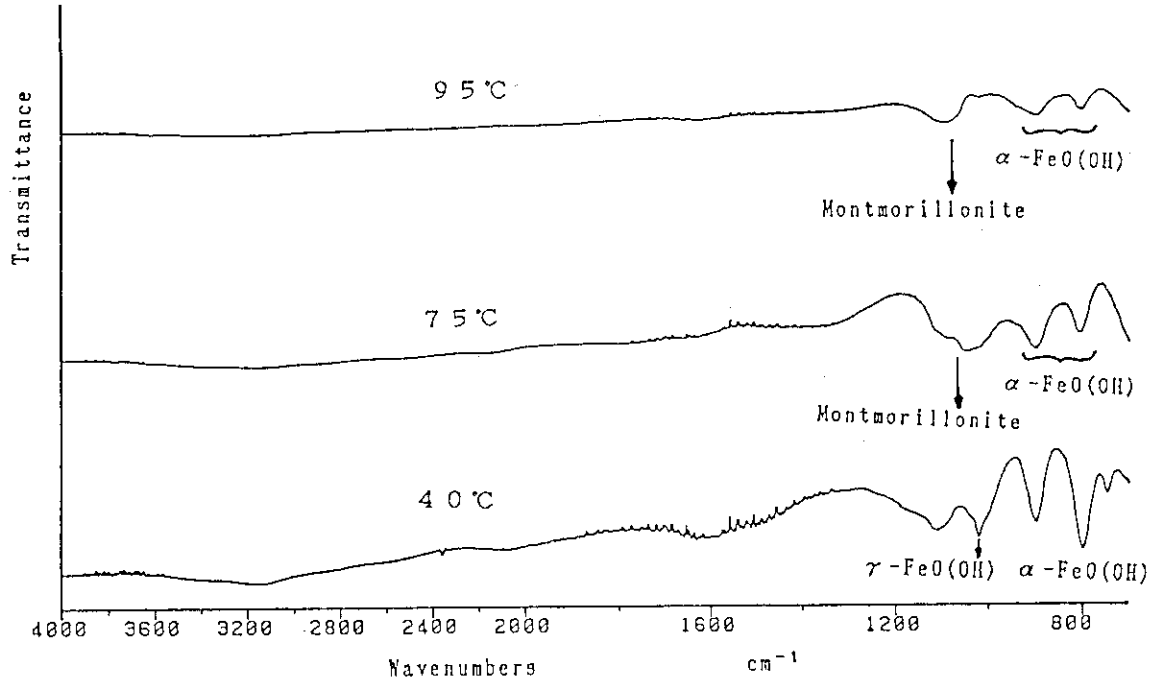

Fig. 2 Analysis of corrosion products in wet bentonite by FT-IR.

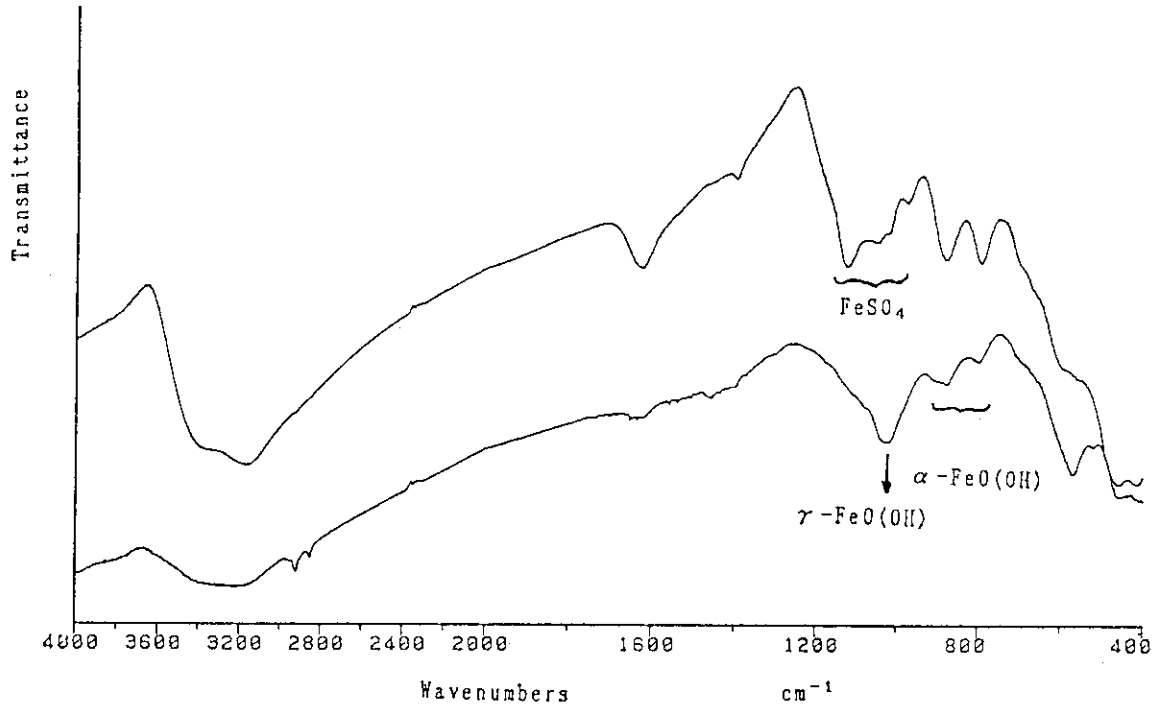

Fig. 3 Analysis of corrosion products in wet bentonite at 95°C by FT-IR.

2. Safety evaluation study for geological disposal

2.1 Chemical behavior of radionuclides in water

2.1.1 Effect of ionic strength on the solubility of neptunium(V) hydroxide

H. Itagaki and S. Nakayama

Introduction

Chemical behavior of neptunium in near-neutral aqueous solutions is dominantly determined by its hydrolysis and carbonate complexation reactions[1]. Therefore, exact data on the solubility, hydrolysis constants and complexation constants are needed to predict the behavior in natural waters. The hydrolysis of neptunium(V) and the solubility of the hydroxide, NpO_2OH, have been studied by several researchers, and many sets of the solubility product and hydrolysis constants have been obtained[2-12]. However, the experiments were carried out for different ionic strengths, and the dependence on the ionic strength has not been systematically understood.

In the solubility measurement, solubility-controlling solid should be primarily speciated because solubility depends strongly on the state of the solid phase. Strickert et al.[13] found that freshly-prepared amorphous neptunium(IV) hydrous oxide, $NpO_2 \cdot xH_2O$, aged to crystalline NpO_2 of lower solubility within one month. The crystallinity of solid phase may change the solubility.

We studied hydrolysis of neptunium(V) hydroxide under the oxidizing condition in the pH range of 7 to 12. The objectives are to obtain the dependence of the solubility on the ionic strength of aqueous phase, and to determine the state of the solubility-controlling solid phase. Our experiments are in progress. The mathematical formulation for the ionic strength-dependent solubility product and hydrolysis constants will be given later.

Experimental

Reagents

The neptunium-237(^{237}Np) stock solution was prepared from neptunium dioxide powder (NpO_2,>99wt%, CEN, Fontenay aux Roses, France). The powder was dissolved in concentrated HNO_3, fumed to near dryness, and the residual was dissolved in 1M $HClO_4$. The neptunium concentration of the final stock solution was about 1×10^{-2} M.

Deionized water used in the experiments was deaerated by boiling. A NaOH solution was prepared from reagent-grade pellets of NaOH and the deaerated deionized water. Carbonate contained in the NaOH solution was removed by adding $BaCl_2$ through $BaCO_3$ precipitation[14]. This solution was kept in an inert atmosphere (99.995% Ar) in a glove box. This NaOH solution and $HClO_4$ were used in adjusting the pH of neptunium solutions.

Procedure

All experiments were conducted in a glove box with an Ar(99.995%) atmosphere under room temperature (20-25°C). The Ar gas was passed through a $BaCl_2$ solution before introducing into the glove box to remove CO_2 from the Ar gas. The $BaCl_2$ solution was placed also in the glove box. The inner pressure of the glove box was kept 5 to 10% higher than the outer pressure to prevent air intrusion.

The neptunium solutions were prepared in 20ml-glass vials. The solubility of NpO_2OH was mainly approached from oversaturation direction. The oversaturation direction consisted of adding an excess amount of neptunium from the stock solution to $NaClO_4$ solution and monitering the concentration in the $NaClO_4$ solution until equilibrium is reached. In the undersaturation direction, solids precipitated in the oversaturation direction were separated in one day and dissolved in $NaClO_4$ solution. The increasing neptunium concentration was measured until equilibrium is reached. The ionic strength of the $NaClO_4$ solution was 0.01, 0.10 or 0.8.

Aliquots of the supernatant (about 200μl) were drawn from the neptunium solutions and filtered through a Millipore 10,000 moleculer weight cutoff filter to separate solids from solutions. Fifty microliters of the filtrates were dried on cleaned stainless steel planchettes and the α-radioactivity was measured with 2π gas-flow proportional counter. The filtrates from $NaClO_4$ solutions of 0.10 and 0.8 ionic strengths were diluted before drying to avoid the dried salts, which inhibits exact α-counting. Some of the separated solids were subject to X-ray diffractometry to examine the crystallinity.

Results and discussion

Neptunium concentrations in the oversaturation direction are shown in Fig. 1 as a function of equilibration time. The concentrations in

higher ionic strength solutions (I=0.10) approach the steady-state values more slowly than those in lower ionic strength solutions (I=0.01). Solubilities were calculated from the last two concentrations for each of the results.

The dependence of the solubility on pH and ionic strength is shown in Fig. 2. In the pH range of 8 to 10, the solubility is clearly influenced by the ionic strength. The increase in the ionic strength results in the decrease in the solubility.

No X-ray diffraction peaks were found for all of the analysed solids stored for 1 day to 3 months. This fact implies that neptunium(V) hydroxide, NpO_2OH, precipitated from near-neutral aqueous solutions at room temperature remained non-crystalline for 3 months.

The solubility products and hydrolysis constants will be calculated at the completion of the measurements, and compared with previous values. The mathematical formulation for the dependence of the data on the ionic strength will be also given.

References

1) Kim, J.I.: in Handbook on the Physics and Chemistry of the Actinides, Vol.4, (A.J.Freeman and C.Keller eds.), Elsevier Science Publishers B.V., Amsterdam, p413 (1986).
2) Kraus, K.A. and Nelson, F.: AECD-1864, U.S.At. Energy Commission (1948).
3) Kraus, K.A.: Proc. Int. Conf. Peaceful Uses At. Energy, Geneva 1955, Vol.7, p245 (1956).
4) Moskvin, A.I.: Sov. Radiochem., 13, 700 (1971).
5) Sevost'yanova, E.P. and Khalturin, G.V.: Sov. Radiochem, 18, 738 (1976).
6) Maya, L.: Inorg. Chem., 22, 2093 (1983).
7) Bidoglio, G., Tanet, G. and Chatt, A.: Radiochim. Acta, 38, 21 (1985).
8) Lierse, Ch., Treiber, W. and Kim, J.I.: Radiochim. Acta, 38, 27 (1985).
9) Bucher, J.J. and Edelstein, N.M.: LBL-15056, Lawrence Berkeley Laboratory (1982).
10) Rösch, F., Milanov, M., Hung, T.K., Ludwig, R., Buklanov, G.W. and Khalkin, V.A.: Radiochim. Acta, 42, 43 (1987).

11) Nakayama, S., Arimoto, H., Yamada, Y., Moriyama, H. and Higashi, K.: Radiochim. Acta, 44/45, 179 (1988).

12) Nagasaki, S., Tanaka, S. and Takahashi, Y.: J. Radioanal. Nucl. Chem., 124, 383 (1988).

13) Strickert, R., Rai, D. and Fulton, R.W.: ACS Symp. Ser., 246, 135 (1984).

14) Rai, D., Swanson, J.L. and Ryan, J.L.: Radiochim. Acta, 42, 35 (1987).

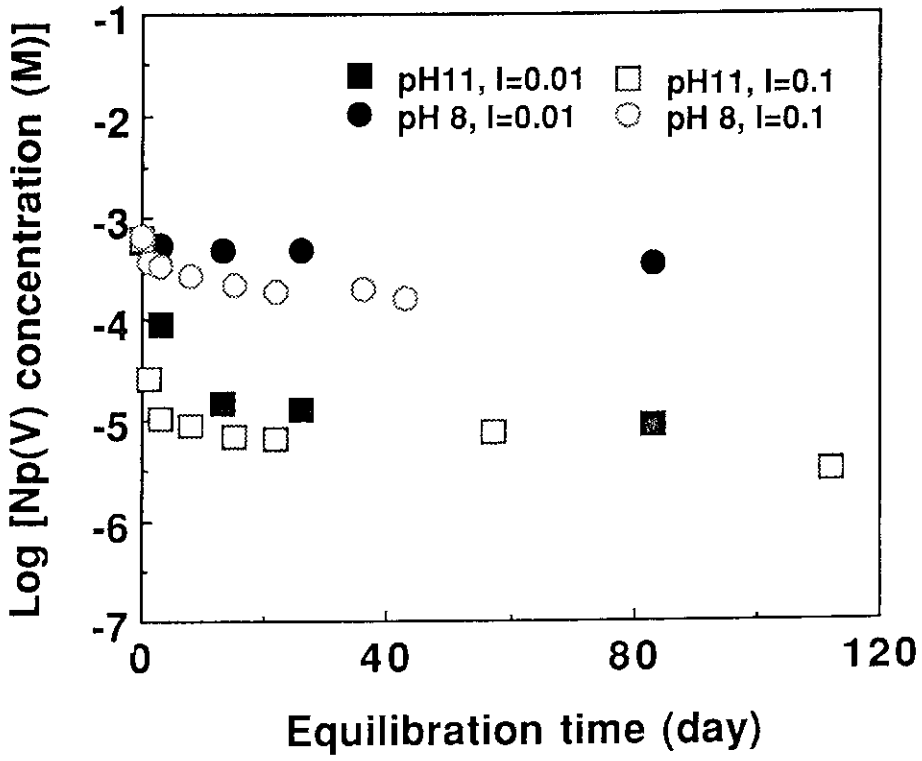

Fig. 1 Neptunium(V) concentrations in the oversaturation direction as a function of equilibration time.

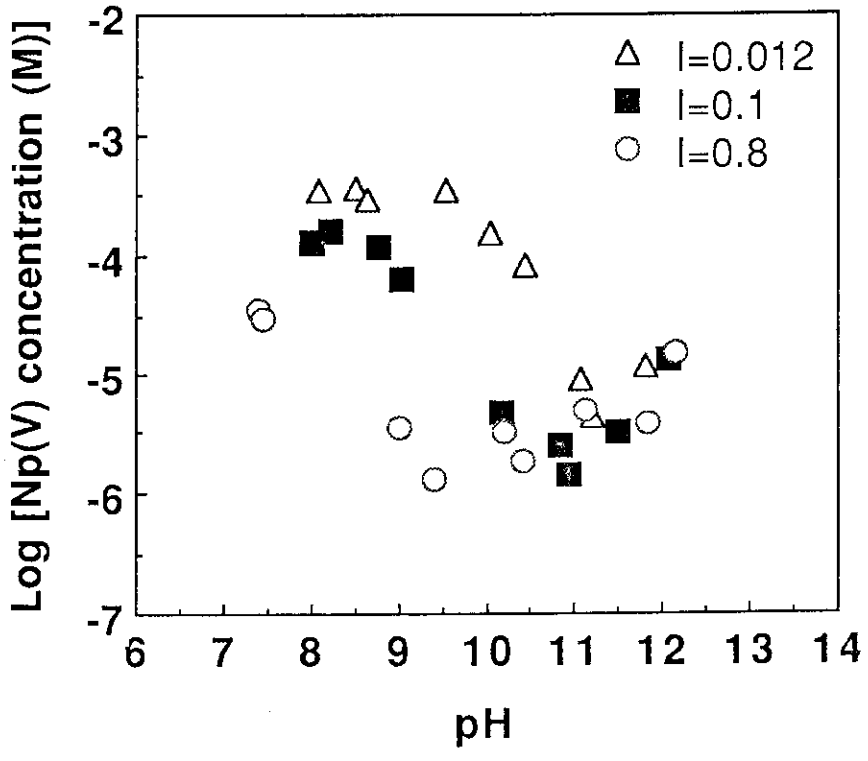

Fig. 2 The solubility of amorphous neptunium(V) hydroxide at room temperature. Effect of pH and ionic strength.

2.1.2 Chemical speciation test of radionuclides in groundwater under in-situ conditions

Y. Sakamoto and R.W.D. Killey

Introduction

In 1960, 25 nepheline syenite glass blocks containing 1100 Ci of mixed fission products and small amounts of actinides were buried in a sand aquifer on the property of the Chalk River Laboratories (CRL) of Atomic Energy of Canada Limited (AECL). The experiment was designed to study glass leaching and radionuclide transport behavior under in-situ conditions. In 1990, under a cooperative agreement between the JAERI and AECL (The Agreement for Cooperation in Field Programs for Research and Development in Radioactive Waste Management), the program was established to update studies of radionuclide release and transport at the Glass Block site. As one part of this project, large volume column packed bed columns were used to determine the chemical forms of radionuclides in groundwater downgradient of the glass blocks.

Experimental

The large volume water sampling column which was developed by Battelle Pacific Northwest Laboratory[1] was used to investigate the speciation of radionuclides in groundwater under in-situ conditions. The column consists of 0.45 μm filter and three sorption beds (20 cm diameter × 2.5 cm thick) as follows; 1) cation exchange resin, Dowex 50×8 Na^+ form, 200-400 mesh, 2) anion exchange resin, Dowex 1×8 Cl^- form, 200-400 mesh, 3) activated aluminum oxide (neutral alumina, AG-7, 100-200 mesh). The activated alumina removes dissolved, uncharged, species.

Groundwater was sampled from two multi-level piezometers installed in 1983 on the center line of the contaminant plume, 1 and 5 m downgradient of the glass blocks. Approximately 100 L of groundwater (pumped at a rate of 270 ml/min) was passed through the column. After collection, the filter and packed beds were removed separately. Radionuclides were extracted with 10 N hydrochloric acid, and gamma and beta activities were determined for each fraction.

Results

The only identifiable radionuclides in the column fractions were ^{90}Sr, ^{137}Cs and ^{241}Am. Figure 1 displays the results of the speciation tests. ^{90}Sr was the dominant radionuclide in terms of abundance, almost all of the ^{90}Sr was present as a cation, as predicted by thermodynamic data. Americium was present only as an anion. Any cationic ^{241}Am would be expected to sorb strongly to aquifer sediments - thermodynamics would not predict any anionic species, leaving us to suggest that the mobile form observed at the Glass Block site is a complex with natural dissolved organics. Although some anionic ^{137}Cs was found in the sample collected 1 m downgradient of the blocks, most of the cesium was sorbed to particles, in agreement with previous tests[2]. At a distance of 5 m from the blocks, however, most of the ^{137}Cs was retained on the anionic exchange resin. These results are interpreted as evidence of filtration of the particulate ^{137}Cs species during transport through the aquifer, leaving only the anionic species still mobile at the 5 m distance.

Acknowledgment

We would like to acknowledge the assistance of J.H. Munch in groundwater sampling.

References

1) D.E. Robertson, Evaluation of a Large Volume Water Sampling Technique for Determining the Chemical Speciation of Radionuclides in Groundwater, (R.A. Bulman and J.R. Cooper Eds.) Elsevier Applied science Publishers, 47, (1985).

2) D.R. Champ and W.F. Merritt, Particulate Transport of Cesium in Groundwater, AECL-7440 (1981).

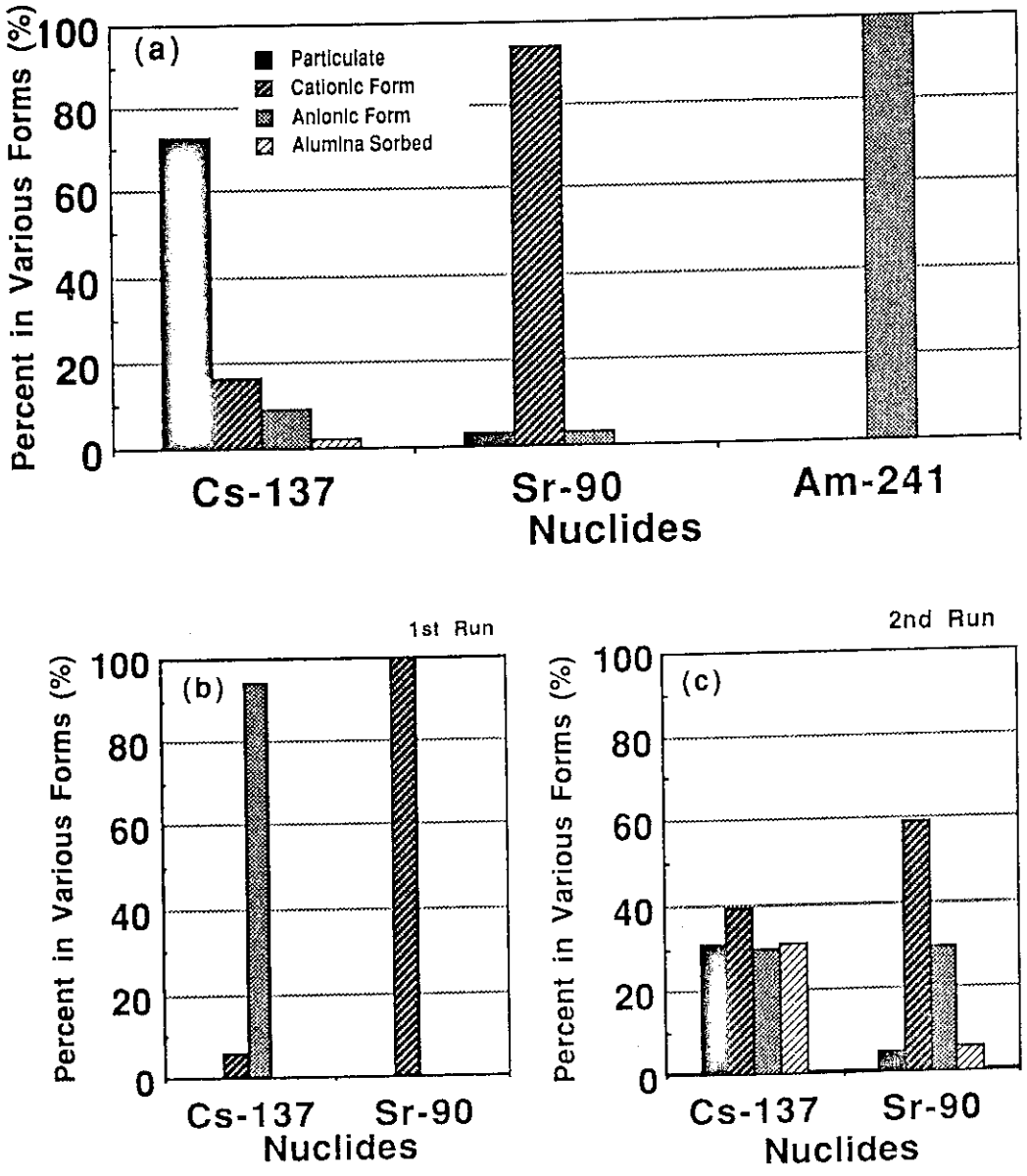

Fig. 1 The fraction of each chemical form of Cs, Sr and Am.
(a): 1m downgradlent from glass blocks
(b): 5m downgradlent from glass blocks (1st Run)
(c): 5m downgradlent from glass blocks (2nd Run)

2.2 Nuclide migration and retardation

2.2.1 Radionuclide migration pathways in fractures of rocks as analysed by the fractal geometry

T. Merceron and S. Nakashima

Fractal analysis can be used to characterize the distribution of fracture fields in rocks, which represent main pathways for material migration such as groundwater flow. Cantor's dust method of the fractal geometry allows to describe quantitatively complex fracture patterns (Velde et al., 1990). The probability of fracture occurrence will be measured to know if they have a fractal distribution. Research program is composed of six successive steps (Fig. 1).

1) The basis of the fractal analysis is that events occur in the same patterns on different scales of observation (Mandelbrot, 1982) and most fractal analysis methods use a means of scaling in order to determine the fractal relation. Different type of fracture fields were analysed to verify if their distribution is fractal in nature. If the distribution is self-similar (fractal), useful predictive methods can be built up to investigate radionuclide migration at larger scales around radioactive waste repository.
2) The validity of the fractal concept for fracture distribution was investigated in a well-known Pb-Zn mine deposit located in the Green Tuff region (Toyoha mine, Hokkaido Japan) at different scales of observation ranging from the thin section to the LANDSAT map. Fracture fields distribution is fractal in the Toyoha district up to a scale factor of 10^6 (Merceron and Velde, 1990).
3) Fracture distribution was analysed in Takigami drill-hole (Oita, Kyushu) by using fractal geometry on a continuous depth interval in volcanic rocks in order to check the validity of the fractal concept Fracture distribution appears to be fractal. However, variations of the fractal dimension have not been explained because of the superimposition of different fracture style and lacking of structural data.
4) Further fractal investigations of fracture distribution were performed on granite along Auriat scientific borehole (Massif Central, France). Various modes of ruptures in the granite were distinguished after dip sorting of fractures available from structural data along 1,000 m depth. Shear, tension and

compressional fractures were treated by using fractal analysis. Detailed results will be completed in near future.

5) Fractal results obtained in Auriat must be compared with other fractal data from different geodynamic and geolgical settings. Shikoku and Oku-Aizu drill-cores in Japan and other granitic occurrences in Butte mining district (Montana, USA) will be examined. Figure 2 illustrates the fractal distribution of fractures in the Shikoku drill core.

6) The main goal of our study is to correlate our fractal results with other geophysical parameters recorded along drill-holes such as permeability, resistivity etc...

Fractal analysis appears as a powerfull method to describe fracture distribution in various rocks at different scales of observation ranging from cm to several km. This method will be used to built up predictive models of radionuclide migration around radioactive waste repository.

References

1) Mandelbrot, B.B. (1982) Fractal Geometry of Nature. Freeman, N.Y., 468 pp.

2) Merceron, T. and Velde, B. (1990) Application of Cantor's dust method for fractal analysis of fractures in Toyoha mine (Hokkaido, Japan). Submitted to Journal of Geophysical Research.

3) Velde, B., Dubois, Badri, A. and Touchard, G. (1990) Fractal analysis of fractures in rocks: The Cantor's dust method. Tectonophysics, 179, 345-352.

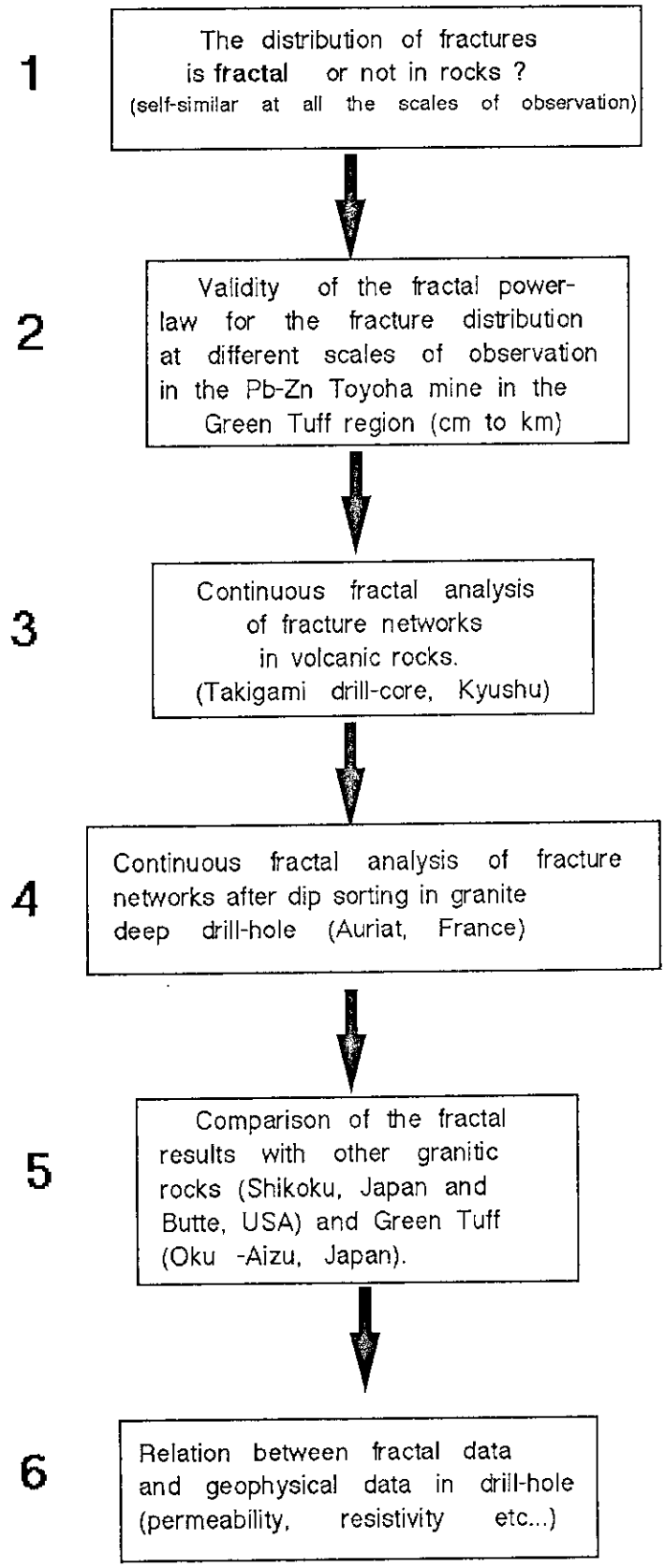

Fig. 1 Research program for the fractal analysis of fractures of fractures in rocks.

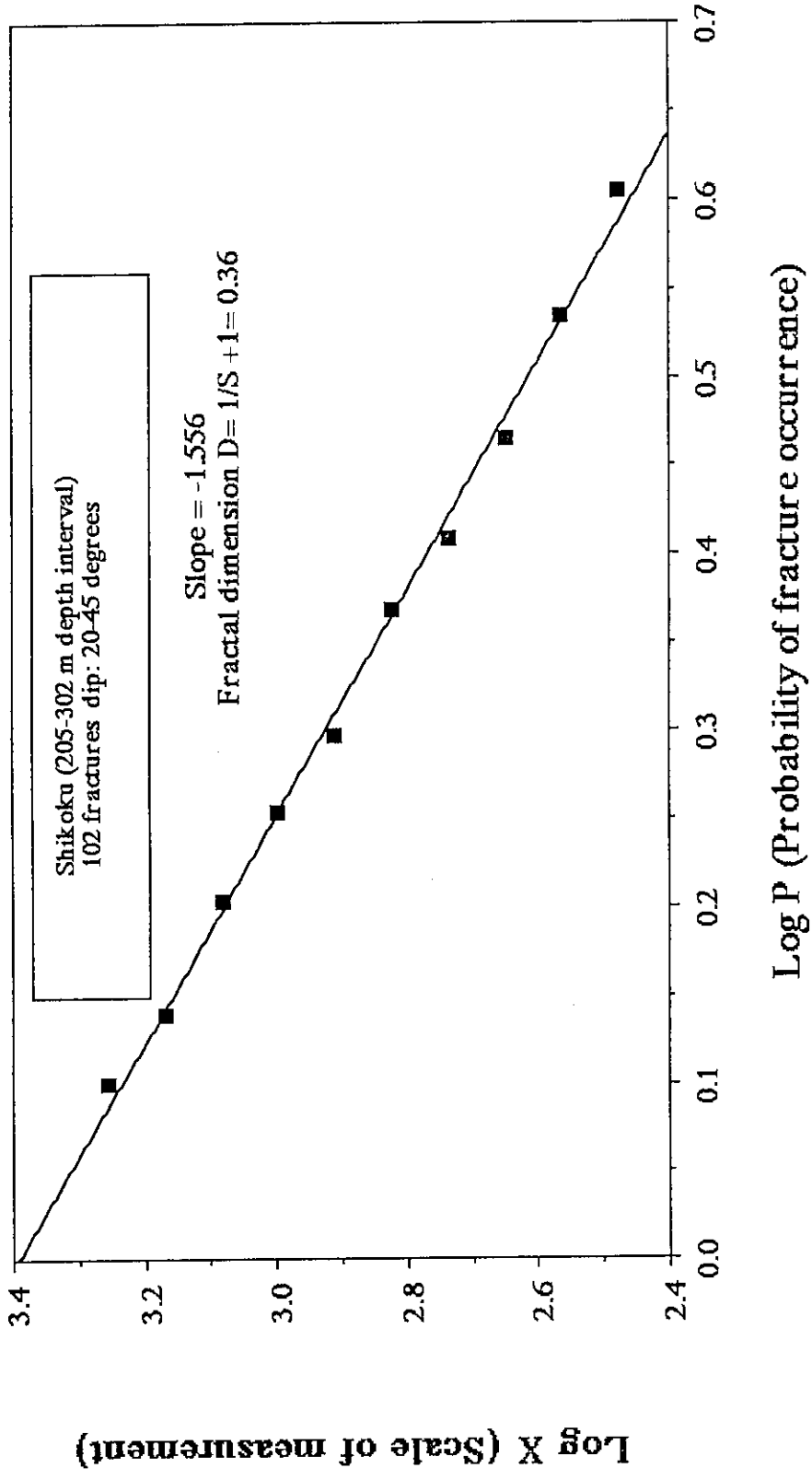

Fig. 2 Log P versus log X diagram showing the fractal relation for the fracture distribution in Shikoku.

2.2.2 Column test for technetium in the URL, Canada

M. Kumata

Introduction

The geochemical processes such as diffusion, oxidation-reduction kinetics, colloid formation and precipitation may play an important role in the transport of radionuclides. In order to predict the transport of specific nuclides from a vault of high level radioactive wastes under deep geological conditions, experimental efforts should be make under realistic conditions. Generally, reducing conditions are expected in deep underground. On the other hand, technetium, one of the important long lived radionuclides contained in high level radioactive wastes, is potentially quite mobile in an aqueous environment. In its oxidized form (VII), technetium is a highly soluble, anionic aqueous species. However, under reducing conditions technetium exists in the (IV) oxidation state and is quite insoluble and highly sorbing.

Considering with these circumstances, a new experimental system which would be able to perform column tests and diffusion tests under realistic conditions was developed under a JAERI/AECL cooperative program. The experimental system was installed in a experimental room excavated specially for the program at a 240 m level of the Underground Research Laboratory (URL) in Canada. The URL is constructed in Precambrian batholith outcropped near Pinawa, Manitoba.

A column test for technetium was carried out in this experimental system by using crushed granitic rock and real groundwater obtained from a fracture zone at a depth about 250 m.

Experimental

The experimental system was designed to maintain the original geochemical conditions of rock and groundwater which will be used in the experiments. A controlled atmosphere glove box was set in the room (Photo.1). Nitrogen gas was used to maintain an inert atmosphere within the glove box. The oxygen content of the glove box was reduced to a few ppm by volume.

A new borehole was drilled from in front of the room to a fracture zone extending in granitic rock. Pink colored granitic rock core was recovered from the borehole and the most highly fractured

sections of the core was selected for the column tests (Photo.2). This material was wet-crushed, using deoxygenated groundwater from the fracture zone, in a jaw crusher equipped with tungsten carbide jaws. Then, the material was wet-sieved using groundwater from the fracture zone in stainless steel sieve trays into several fractions. The 180-850 μm fraction was selected for the column tests. During these procedure, the rock samples were handled carefully to minimize contact with air.

The groundwater was directly introduced into the system from the fracture zone through the borehole to supply the water without contact to air. Chemical composition of the groundwater from the borehole is shown in Table 1. During the experimental period, Eh, pH, conductivity, temperature and pressure of the groundwater were monitored by an on-line system in the experimental room. The water was supplied for the column tests at a pressure reduced to 0.7 MPa.

The columns used in this experiments were made by stainless steel sized 2.54 cm in diameter and 20 cm in length. The column surface was carted with Teflon (Photo.3). The solution containing the radionuclides is injected at a pressure of 0.7 MPa by the supplied groundwater using a hydraulic accumulator. The flow rate was controlled by a timer device which co-ordinates the operation of the solenoid valves.

For gamma scan of the column, technetium-95 m, short lived gamma nuclide, was used instead of ^{99}Tc, long lived nuclide. Tritium was used as a non-reactive tracer and injected with technetium simultaneously. The injection solution for the technetium column test was prepared in a surface laboratory as follows: the appropriate amounts of a stock technetium solution ($NH_4{}^{95m}Tc$) and of a highly tritiated D_2O solution were left in an anaerobic chamber for about one week. The technetium solution and the tritiated D_2O were then added to about 250 ml of the groundwater in the anaerobic chamber. The groundwater from the borehole has been equilibrated with the atmosphere in the anaerobic chamber.

About 150 ml of the ^{95m}Tc and tritium mixture solution was injected in to the column. The column was gamma scanned periodically over a period of four months.

Results

A very small fraction (< 10 %) of the injected technetium was recovered from a tritium breakthrough region (Fig. 1) and the remaining fraction of the injected ^{95m}Tc was strongly retarded in the column. Periodic gamma scanning of the column showed no movement of the ^{95m}Tc through the column. This suggests that the technetium was sorbed very strongly on the geological material in the column.

After four months duration of the column operation, the column was removed to recover the column material. The column was frozen, then it was slightly warmed and the frozen column material was sliced into 1 cm-long sections. These samples were dried and analyzed by gamma spectrometry. The results are shown in Fig. 2. The technetium appeared to have precipitated or sorbed on the mineral particles near the inlet of the column. Some of the material from the inlet of the column was prepared for analysis by autoradiography. The autoradiographs showed that the activity was associated with dark of mafic minerals. This means preferential sorption of the technetium on the column material.

Table 1 Chemical composition of the groundwater from the borehole.

element	conc.(mg/l)
Na	190.
K	0.71
Ca	3.6
Mg	0.31
Fe	0.037
Si	3.58
Al	< 0.1
Sr	0.053
HCO_3	220.
Cl	125.
SO_4	51.9
Br	9.
NO_3	< 0.1
NH_4	< 0.1
TOC*	1.05

*TOC=Total Organic Carbon

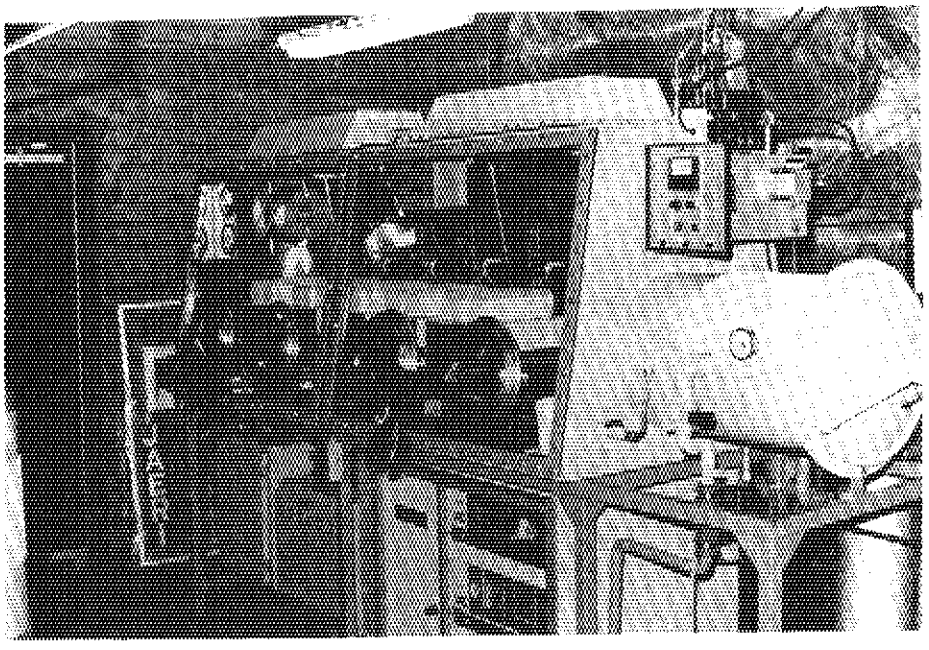

Photo. 1 Glove box installed in the experimental room in URL.
Nitrogen gas was used to maintainan inert atmosphere in it.

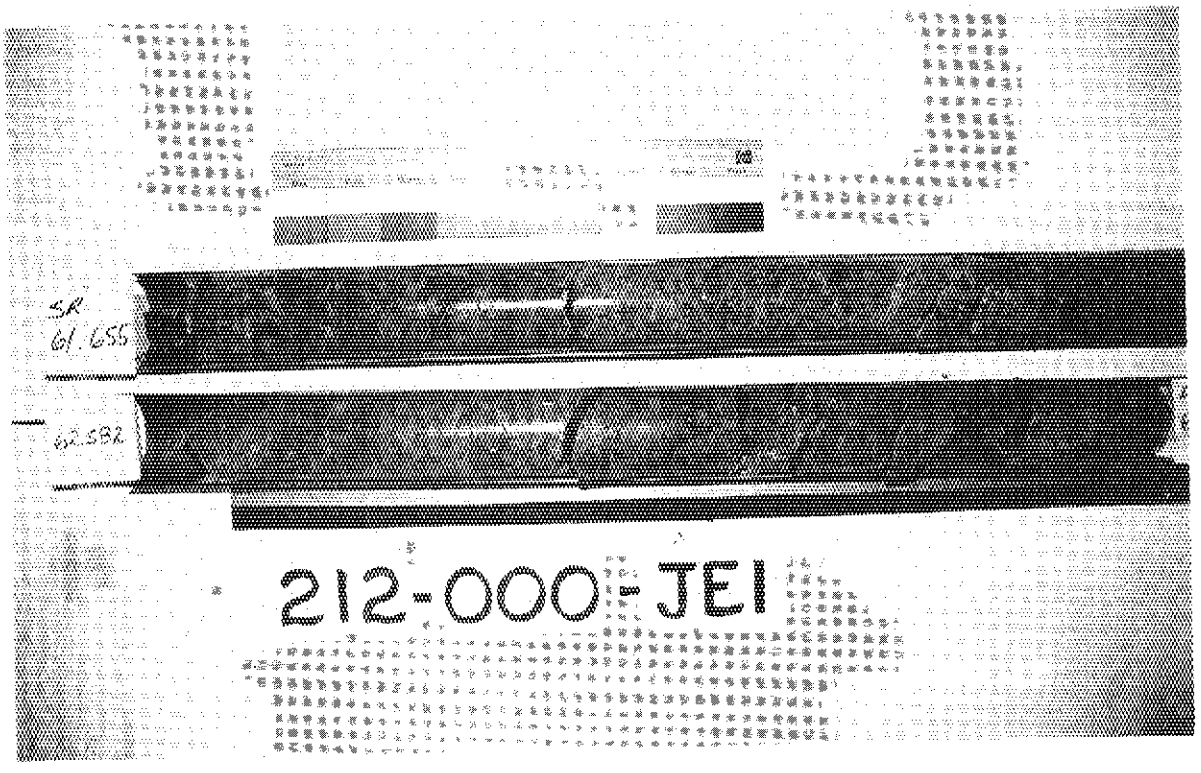

Photo. 2 Core obtained from the fracture zone.
The most highly fractured sections was selected for the column test.

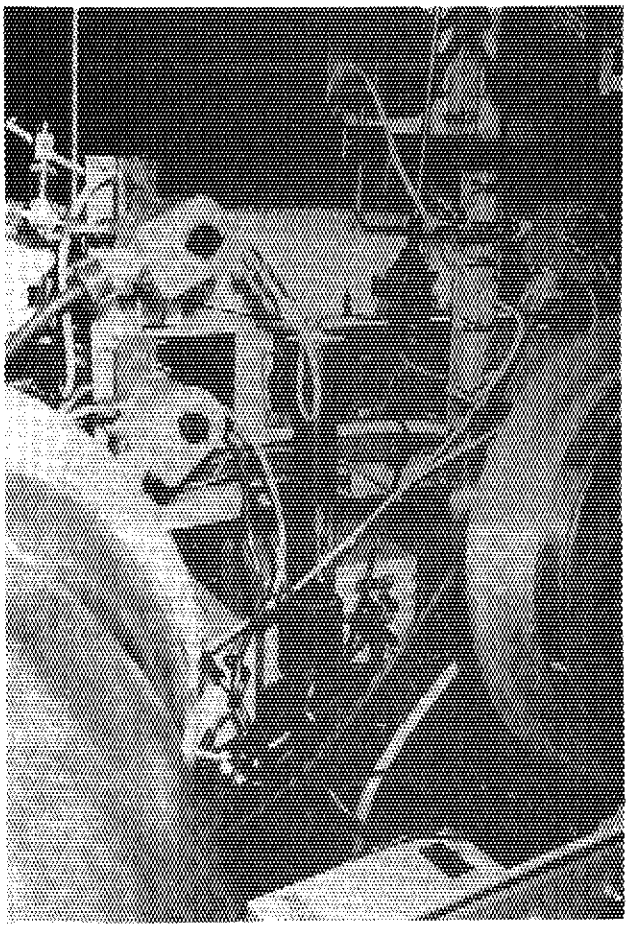

Photo. 3 Colum attached in flame set in the glove box. The surface of the column was carted with Tefion® and colored black.

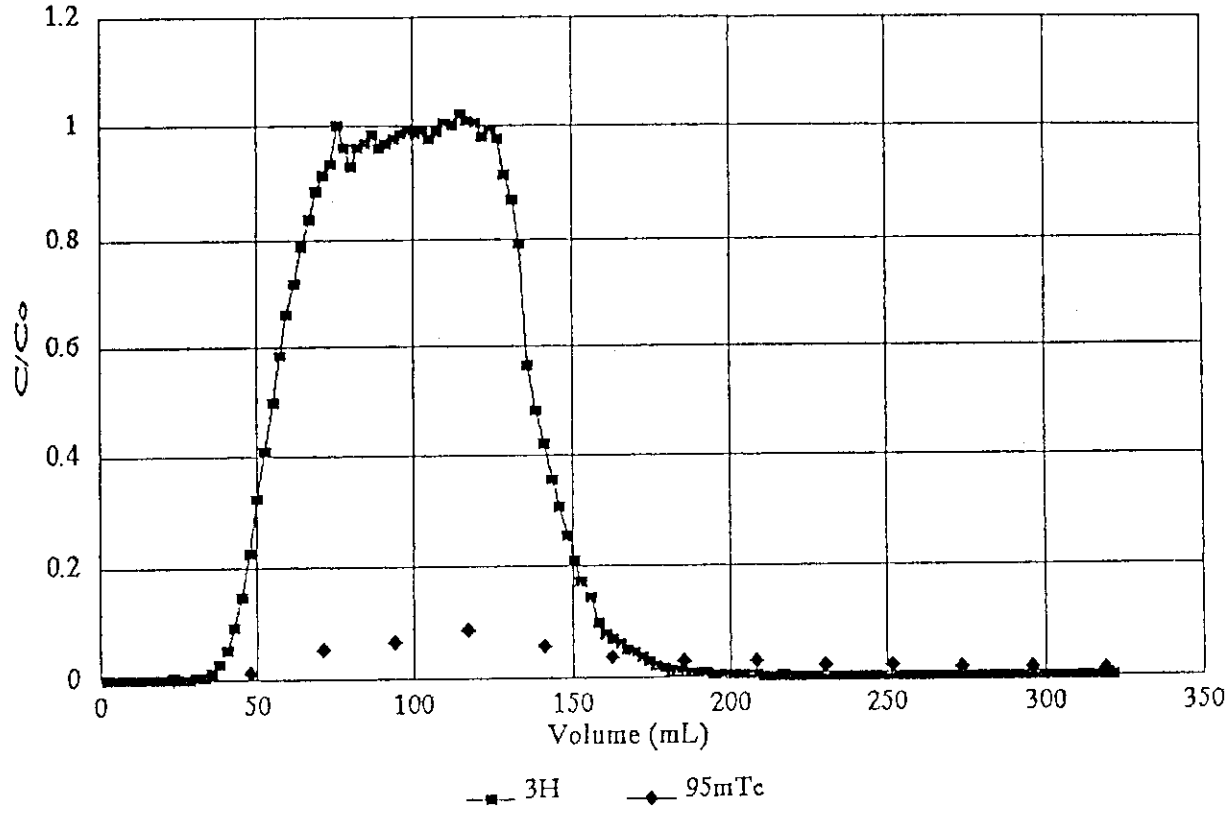

Fig. 1 Technetium-95m and tritium breakthrough courve.

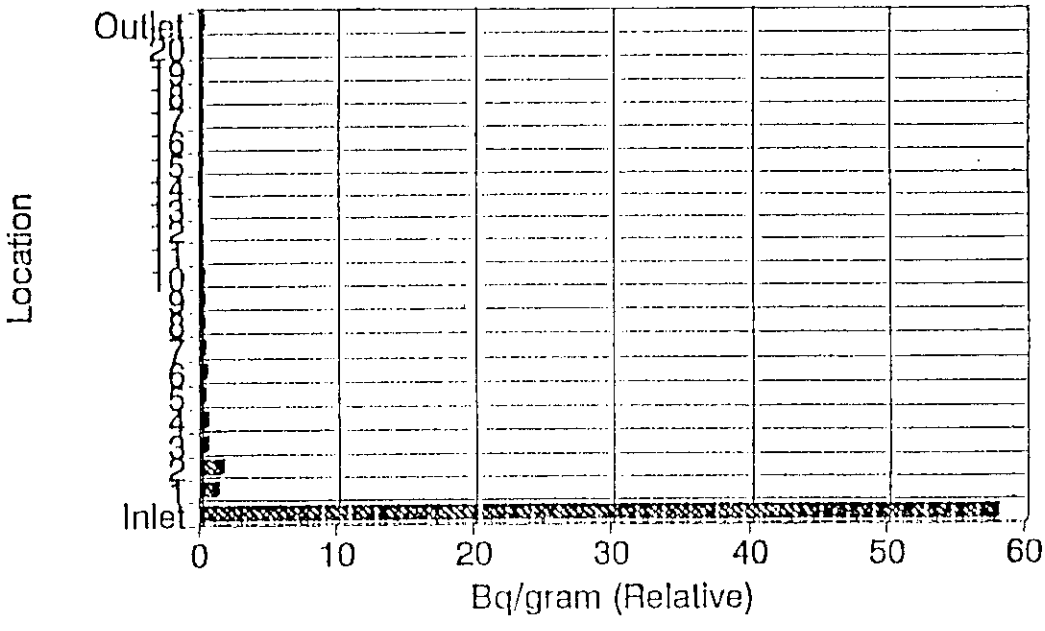

Fig. 2 Technetium-95m distribution within the column.

2.2.3 Fixation of neodymium by coprecipitation with iron compounds

T. Nagano

Introduction

Deep groundwaters around repositories of high-level radioactive wastes are considered to contain a large quantity of iron dissolved from engineered barrier materials such as canister or overpack. Some radionuclides leached from waste glasses are expected to be incorporated into their structures by coprecipitation with the iron, and have certain chemical stability in the geological disposal environment. Consequently, it is very important to study interactions between iron compounds and radionuclides such as transuranic (TRU) elements. However, these studies are very limited till now [1], [2]. In this study, as the first step to elucidate fixation mechanism of TRU elements by iron compounds, coprecipitation experiments of neodymium (Nd) with iron (Fe) were conducted to investigate effects of molar Nd/(Nd+Fe) ratios in initial solutions on the fixation mechanism of neodymium by iron compounds. Neodymium was chosen because of the similar valence and an ionic radius in solutions to trivalent TRU elements such as americium.

Experimental

Freshly prepared 0.1 M ferric perchlorate solutions and 0.1 M neodymium perchlorate solutions were mixed in 250 ml polyethylene bottles at different molar Nd/(Nd+Fe) ratios of 0, 0.1, 0.5, 1, 3, 5, 7, 10, 15, 30, 50, and 100 %. The pH of the solutions were adjusted to 9.0-9.5 by adding ammonia. The solutions were stirred continuously during the pH adjustment to avoid local precipitation. The suspensions were kept in a thermostated oven at 70°C for about 1 week. The precipitates were then centrifuge-washed two times with deionized water before being freeze-dried.

Crystalline phases of the resulting precipitates were characterized by X-ray diffractometry (XRD) using Rigaku powder diffractometer (CuK_{α} radiation). In order to examine the chemical states of neodymium in the coprecipitates, detailed analyses were made by fourier transform infrared spectroscopy (FT-IR), differential thermal analysis (DTA) and XRD.

Results and Discussion

XRD analyses of the bulk samples revealed that the coprecipitate phases were different according to the molar Nd/(Nd+Fe) ratio in the initial solutions, i.e. a) goethite (FeOOH) and hematite (Fe_2O_3) (the ratio of 0-10 %), b) amorphous materials (15-30 %) and c) neodymium hydroxide ($Nd(OH)_3$) (50-100 %). Figure 1 represents the correlation between the iron compound crystallinity and the logarithm of Nd/(Nd+Fe) ratio. The crystallinity of the iron compunds was determined by relative heights of the XRD peak at 2.70 A, which is a common peak of goethite and hematite. In this figure, it is found that the initial solutions with higher Nd concentration resulted in the formation of iron oxides with less crystallinity. This result is a clear evidence that Nd prevents the crystallization of iron oxides.

Chemical states of neodymium in goethite of the a) region were examined by FT-IR and those in the amorphous materials of the b) region by DTA and XRD. Infrared spectra for lower Nd/(Nd+Fe) ratio samples (0-10 %) exihit the distinct Fe-OH bending vibrations associated with goethite around 800 and 900 cm^{-1}. Figure 2 represents infrared spectra for the samples of the initial Nd/(Nd+Fe) ratio between 0.5 and 7 % (labeled as FN0.5 to FN7) in the wavenumber region of 750 to 950 cm^{-1}. In this figure, intensities of these two peaks apparently decrease as the ratio increases in accordance with the previous XRD analyses. Moreover, Fig. 2 indicates an interesting result that the positions of both two peaks slightly shift to lower wavenumber regions, i.e. from 898.7 to 890.0 cm^{-1} or from 804.2 to 797.4 cm^{-1}, as the ratio increases. It is a well-known phenomenon that when a constituent cation of an oxide or hydroxide with the same crystal structure has larger atomic weight, vibration frequencies of the crystal take smaller value than those with smaller cation, and consequently the equivalent peak shifts to lower wavenumber region. Therefore, it can be said that the slight shifts of goethite infrared peaks to the lower wavenumber region around 800 and 900 cm^{-1} means that parts of constituent iron of goethite were replaced by neodymium which has a larger atomic weight than iron. Consequently, some parts of neodymium can be considered to be fixed in goethite-like structures.

DTA curves for the amorphous precipitates with the Nd/(Nd+Fe) ratio of 15 and 30 % indicate that two exothermic reactions occurred at around temperatures of 200 and 700°C. In order to identify these

thermal changes, the amorphous samples were baked in an oven at 300°C for 1 week and at 850°C for 4 hours and then characterized by XRD. XRD analyses for the samples heated at 300°C showed similar amorphous patterns to the initial precipitates, but those at 850°C show sharp peaks of a new crystalline phase, $FeNdO_3$, and weak peaks of hematite. From this result, the chemical reactions occurred around 700 °C can be production reactions of $FeNdO_3$ and hematite from the amorphous materials. This result suggests that the amorphous precipitates (the ratio of 15-30 %) are not composed of independent compounds of iron and neodymium but of Nd-bearing iron hydroxides. In the other words, neodymium was fixed as the amorphous Nd-bearing iron hydroxides in this region.

All these results suggest that neodymium can be fixed by amorphous iron compounds up to significant molar Nd/(Nd+Fe) ratios in the initial solutions. For a quantitative explanation of a long-term interaction mechanism between neodymium and iron compounds, further examination about the evolution in time of neodymium-bearing iron compounds is necessary in the future.

References

1) Walton, F.B., Paquette, J., Ross, J.P.M. and Lawrence, W.E., Tc(IV) and Tc(VII) interactions with iron oxyhydroxides, Nuclear and Chemical Waste Management, Vol.6, 121-126, 1986.

2) Goncharova, L.K., Myasoedov, B.F. and Novikov, A.I., Sorption of americium in different oxidation states by iron and zirconium hydroxides, Radiokhimiya, Vol.16, 308-312, 1974.

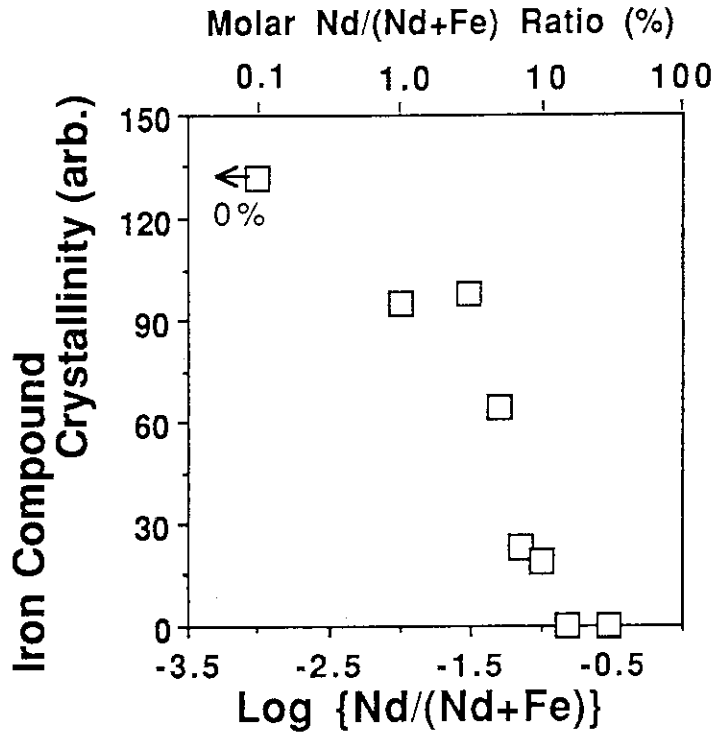

Fig. 1 Correlation between iron compound crystallinity and logarithm of molar Nd/(Nd+Fe) ratio. The crystallinity is determined by an XRD peak at 2.7 A, a common peak of goethite and hematite.

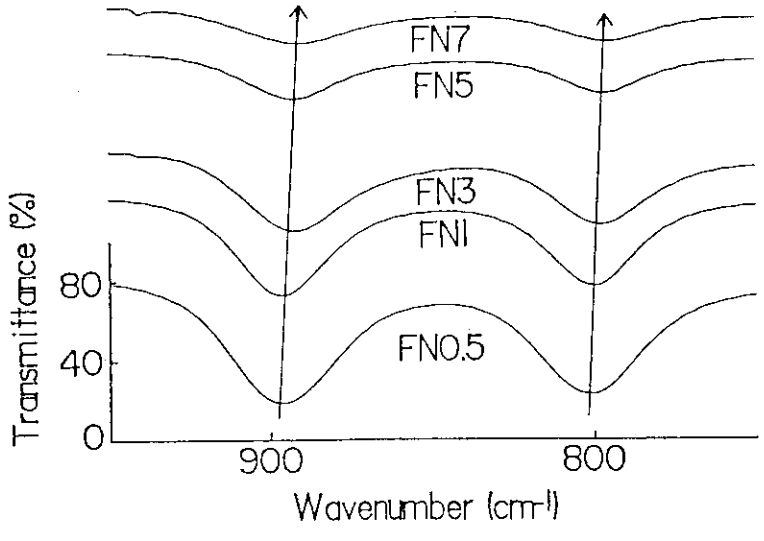

Fig. 2 Infrared spectra for coprecipitates of iron and neodymium in the Nd/(Nd+Fe) ratio range from 0.5 to 7 %.

2.3 Long-term radionuclide fixation mechanisms

In order to study quantitatively the long-term behavior of waste radionuclides in geological environments, kinetic consideration is indispensable because all geological systems evolve in time. The kinetic parameters such as rate constants are very difficult to be determined from the natural system and experimental systems generally treat only the short period. It is then necessary to clarify reaction mechanisms of radionuclide migration-fixation in natural systems in order to simulate these in laboratory experiments.

The first step of this study is to analyze chemical forms of microphases in natural rocks for the purpose of reaction path modeling. New spectroscopic methods have been developped for the microphase characterization. The second approach is the simulation experiments of radionuclide fixation by iron hydroxides which are the main products of low temperature water-rock interactions in nature.

2.3.1 Fourier transform visible-near infrared-infrared microspectroscopy of geomaterials

S. Nakashima

Introduction

Spectroscopic methods are considered to be most suitable for the study of chemical forms of elements in rocks. However, conventional spectroscopic methods are not able to analyze non-destructively chemical speciation in microscale. Development of new microspectroscopic methods are hence needed. We have already succeeded in developping Fourier transform infrared microspectroscopy (Abreviated as Micro FT-IR) for the analysis of hydrous species in rock thin sections in areas as small as 10 μm [1,2]. It is then desirable to have further information on chemical forms of iron and uranium on the same type of rock samples in visible and near-infrared regions. In order to extend Micro FT-IR to near-infrared and visible wavelength regions, we have devolopped a new type of multi-microspectrometer.

Experimental

Fourier transform Michelson interferometer Bomem DA3.02 can cover a wide range of wavelength because of its possibility of changing

light sources, beam splitters and detectors by means of Dynamic Alignment of the optical configurations (Fig. 1). We have employed three different assemblies for three different wavenumber regions as in Table 1.

The multi-spectrometer was connected to a microscope having not optical lenses but mirror systems as optics (Spectra Tech IR-Plan) which can be used in the visible to infrared regions (Fig. 1). The rock thin sections are placed over a hole of stainless plates and then put on the sample stage of this microscope. The rectangular aperture is used to mask the image to select desired areas for analysis.

The reference spectra without the sample and then the transmittion spectra on the sample were measured for the three different spectral regions. The ratios of these spectra give three absorption spectra of the sample and these are combined to form a single absorption spectrum of the sample covering from visible to infrared regions.

Results and Discussion

A thin film (21 μm thick) of natural biotite from Nellore, India was first meausred by the above method. This mineral generally has a chemical formula of $K_2(Mg,Fe^{2+}, Fe^{3+}, Al)_{5-6}(Si, Al)_8O_{20}(OH)_4$ and the present sample contains Fe^{2+} (24.5 wt% as FeO) and Fe^{3+} (0.8 wt% as Fe_2O_3). We have succeeded, for the first time in mineralogy and geochemistry, to take VIS-NIR-IR spectra of this sample in areas as small as 100 × 100 μm as shown in Fig. 2. The vibrations of crystal lattices of Si-O around 1000 cm^{-1} and Al-O around 780 cm^{-1} together with different states of O-H stretching at 3595, 3270 and 3020 cm are observed in the infrared. In the near-infrared, electronic absorptions of Fe^{2+} are observed around 1125 and 910 nm. A broad band at 730 nm are considered to be due to the intervalence charge transfer (IVCT) between Fe^{2+} and Fe^{3+} and a band around 520 nm can be attributed to Fe^{3+} in a tetrahedral site. The electronic and molecular structures are hence characterized in microscale for a natural mineral.

A conventional rock thin section (about 30 μm thick) of a granitic rock from Saga, Kyushu, Japan was then analyzed for determining products of hydrothermal alteration in albitized red feldspar (close to $NaAlSi_3O_8$). The glass plate and adhesive are removed with an organic solvent before the analysis. This red feldspar contains fine sericite-like clays determined by Micro FT-IR (1) and submicron iron minerals

such as FeOOH and Fe_2O_3 by visible diffuse reflectance spectroscopy on powders and by transmission electron microscopy (2). The resulting Micro VIS-NIR-IR spectra of red feldspar in 100 × 100 μm area is shown in Fig. 3. Expected infrared bands are clearly observed and a band at 3620 cm^{-1} is considered to be due to sericite and that around 3400 cm^{-1} can be due to other fine clays and/or fluid inclusions (1). In the visible region, two broad bands around 550 and 900 nm are observed and these are considered to be mixture of FeOOH (480-520, 640 and 890 nm) and Fe_2O_3 (550 and 850 nm). Consequently, information on hydrous microphases in the IR region and that on iron-containing microphases in the visible are characterized in a single spectrum.

We have tried to measure spectra in smaller areas than 100 × 100 μm but it was not possible, especially because of the low sensibility in the visible region. In order to develop a high-sensitive compact visible microspectrometer, we have conceived a new type of FT mutichannel spectrometer installed on a normal petrographical microscope. This microspectrometer is composed of a compact interferometer of Wollaston prism and CCD camera and is expected to measure visible spectra from 400 to 950 nm in areas as small as 3 μm and to be able to conduct two-dimensional imaging of rock samples.

All these results suggest that this kind of microspectroscopic methods can be a powerful tool to characterize non-destructively chemical forms of various microphases in terms of electronic and molecular structures. This Micro FT-VIS-NIR-IR can be hence expected to be effective in the long-term reaction path modeling of radionuclide fixation in rocks.

References

1) Nakashima S., Ohki S. and Ochiai, S.: Infrared microspectroscopy analysis of the chemical state and spatial distribution of hydrous species in minerals. Geochem. J., 23, 57-64 (1989).

2) Nakashima S. and Nagano T.: Long-term reaction path modeling of radionuclide fixation in geosphere by spectroscopic methods. Proc. Joint Intl. Waste Manag. Conf. Vol.2, A.S.M.E., New York. 341-346 (1989).

Table 1 Measurement systems of FT spectrometer Bomem DA3 equipped with a microscope Spectra Tech IR-Plan for covering from visible (VIS), near infrared (NIR) to infrared (IR) wavelength regions.

Spectral region	Wavenumbers (cm-1)	Light source	Beam splitter	Detector
VIS - NIR	23000 - 8500	Quartz-Halogen	Quartz	Silicon
NIR - IR	8500 - 1800	Globar	CaF2	InSb
IR	5000 - 800	Globar	KBr	MCT

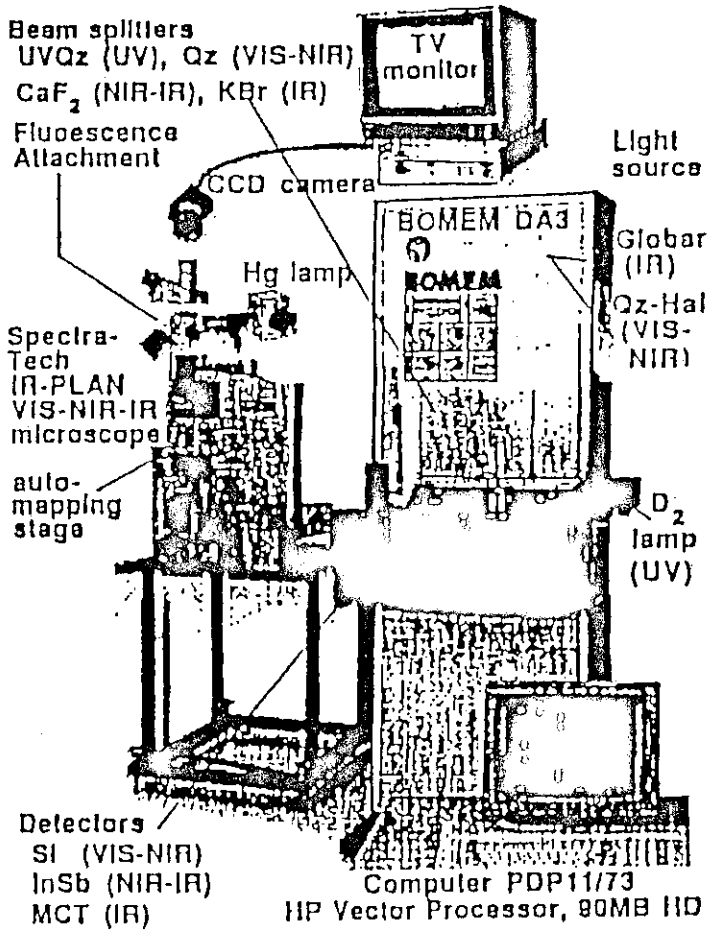

Fig. 1 Schematic system configuration of FT-VIS-NIR-IR microspectrometer.

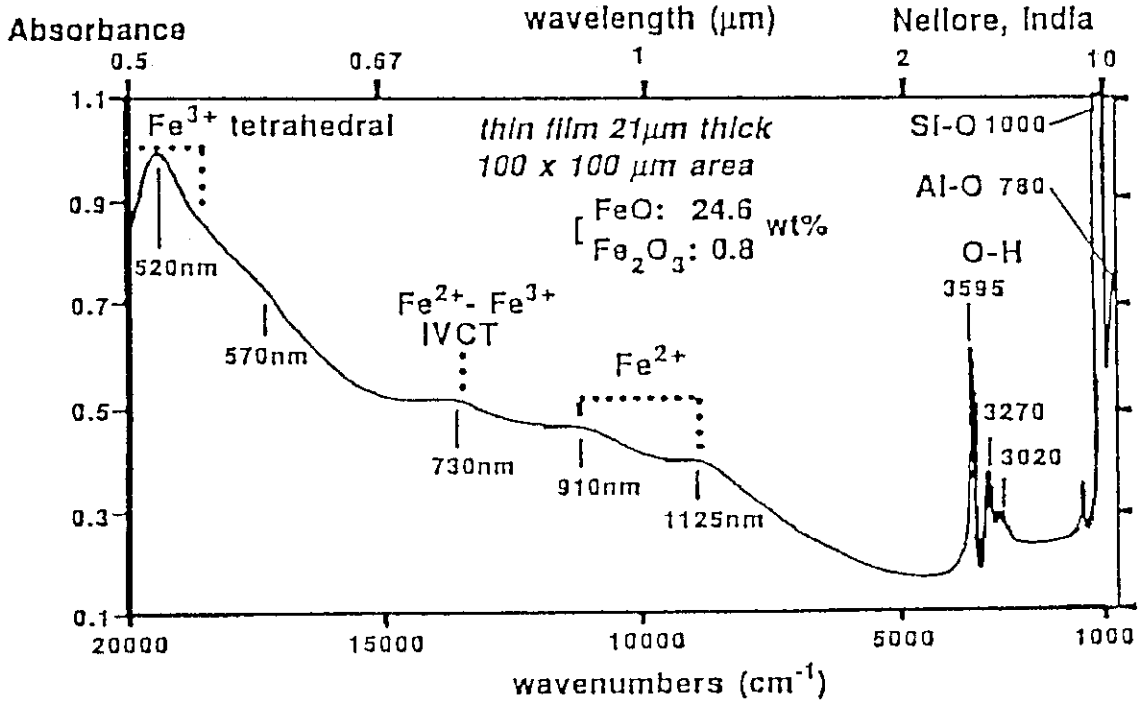

Micro FT-VIS-NIR-IR Spectra of Biotite

Fig. 2 Micro FT-VIS-NIR-IR spectra of biotite, Nellore, India in 100×100 μm area.

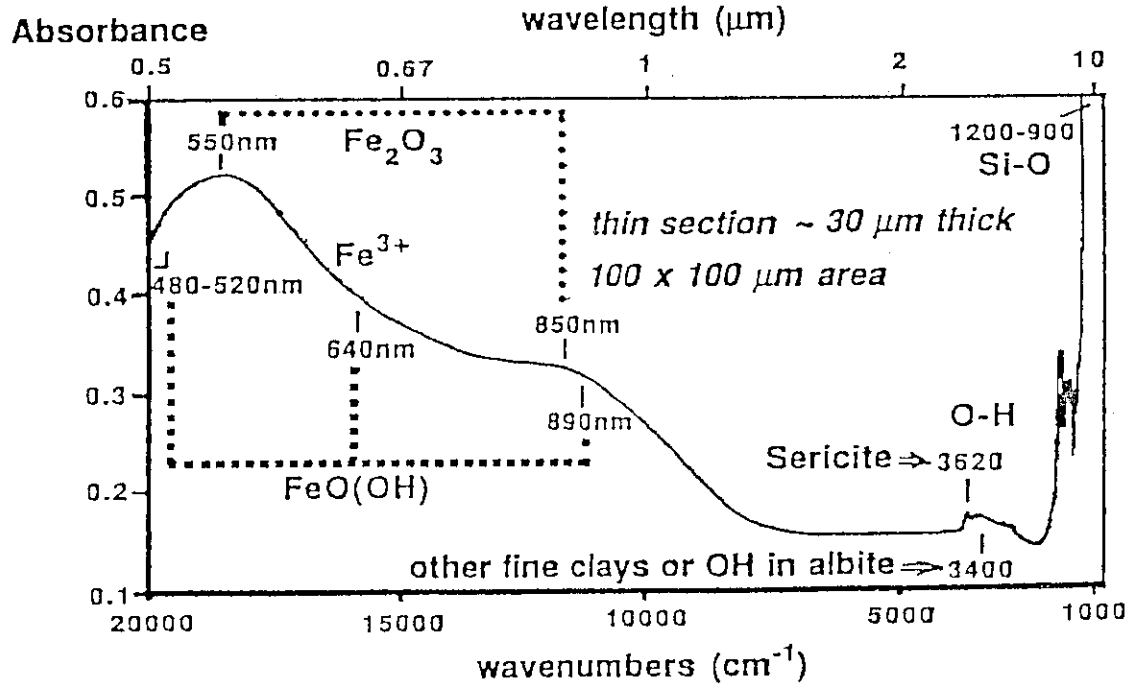

Micro FT-VIS-NIR-IR Spectra of Red Albite

Fig. 3 Micro FT-VIS-NIR-IR spectra of red feldspar in hydrothermally altered granitic rock thin section from Saga, Kyushu, Japan in 100×100 μm area.

3. Natural analogue study

3.1 Alteration of chlorite and its relevance to uranium migration

T. Murakami and H. Isobe

Introduction

Transuranic elements are a major concern for the disposal of high level radioactive waste because of their long-lasting (tens of millions of years) hazard. If we consider radionuclide migration over the above period, the host rocks cannot be static, but are dynamic. The rock-forming minerals will be changed structurally and chemically with time by the water-rock interaction, so-called alteration. The authigenic or secondary minerals formed by the alteration are usually metastable. The attainment of equilibrium may be delayed by as much as 10^7 years, longer than the time required for the safety assessment of high level waste disposal. The relationships between the alteration and transuranic elements are characterized by reactions, especially, adsorption and desorption of transuranic elements to the then co-existent minerals, which vary with time owing to the alteration mechanism and kinetics. This suggests that the retardation of transuranic elements will also vary with time, that is, with the co-existent minerals. Knowledge of the alteration mechanism and kinetics is, therefore, essential if we are to understand radionuclide migration over a long, geologic time.

Koongarra provides us with a good testing site in terms of the relevance of the radionuclide migration to alteration. Quartz-chlorite schist, the host rock, has been subjected to alteration. Quartz persists even in the surface while chlorite has been altered to clay minerals and iron minerals in the weathered zone, which is present below the surface for a depth of about 20 m. Uranium is found to be associated with the altered products of chlorite in the downstream of the secondary ore deposit which is located in the weathered zone.

This preliminary report on our work to examine the alteration mechanism and cation redistribution during the alteration in Koongarra work focusses on the relationship between the alteration and uranium distribution.

Samples and experimental techniques

Thirteen samples were used for the present study. Nine of these were chosen from the DDH3 core, so that we could examine the mineral

profile with depth in detail. However, all samples from depths between 4.5 and 47 m along the DDH3 core were initially inspected by the naked eye. Samples located at depths greater than 25.2 m are not generally altered but alteration does occur along fractures in samples between 25.2 and 24.8 m deep. The alteration then gradually extends into the schistosity in samples between 24.8 and 24.1 m deep and the samples are completely altered at depths less than 24.1 m.

A part of the samples were powdered and then centrifuged to obtain fine-grained clay fractions less than 2 μm in size for the identification of clay minerals in the samples by X-ray diffraction analysis (XRD). Each sample was treated with ethylene glycol and heated at 450 and 600 °C to distinguish one clay mineral species from another. The textures of the samples were examined by optical microscopy (OM) and scanning electron microscopy (SEM), and their compositions, by electron microprobe analysis (EMPA).

Results and discussion

A series of XRD patterns of the clay fractions in the DDH 3 samples indicate the possible existence of chlorite, vermiculite, mica, smectite, and kaolinite for all specimens. On the basis of the criteria used to identify the clay minerals[11], the XRD studies are well summarized; the alteration of chlorite occurs as a function of depth; chlorite is transformed to vermiculite through regularly interstratified chlorite/vermiculite; vermiculite is converted to kaolinite and probably smectite; an iron mineral, possibly ferrihydrite, is formed during the alteration; and goethite and hematite are found in the weathered zone.

The chlorite in the first alteration stage is indicated by its change in color from green to brown, which is due to oxidation of Fe^{2+}. Such grains of altered chlorite, showing a layer texture in SEM images, consist of slabs of chlorite and vermiculite 1 μm thick. Between the slabs an iron phase (possibly ferrihydrite), distinguished by the whitest contrast, occurs as a short slab. The layer texture suggests that the crystallographic orientation of the chlorite structure is retained during the transformation of chlorite to vermiculite. The occurrence of the iron phase reveals that Fe reprecipitation takes place out of the original chlorite during the transformation.

The chlorite compositions are rather consistent; MgO, 9-12; Al_2O_3, 15-19; SiO_2, 24-27; and FeO, 26-34 (in wt%). The chlorite compositions in the present study are lower in Mg and higher in Fe than that given by Gray and Davey[2]. Higher Fe content in chlorite may cause faster vermiculitization because of greater charge imbalance and/or structural distortion owing to the Fe oxidation. This suggestion accounts for the narrow zone (1 m thick) of co-existing chlorite and vermiculite below the weathered zone. The decrease of iron during the transformation from chlorite to vermiculite is remarkable while the decrease of Si, Al, and Mg is much smaller. On the other hand, Ti and K, which are rarely contained in chlorite, are accommodated in vermiculite. If we use average compositions of chlorite and vermiculite to express the reaction from chlorite to vermiculite, the following reaction equation can be written:

$$\underset{\text{(Chlorite)}}{(Al_{1.11}Fe_{2.93}^{2+}Mg_{1.97})(Si_{2.87}Al_{1.13})O_{10}(OH)_8} + 0.24K^+ + 0.06Ti^{4+} \rightarrow$$

$$\underset{\text{(Vermiculite)}}{K_{0.24}(Al_{0.34}Fe_{1.01}^{3+}Mg_{1.55}Ti_{0.06})(Si_{2.61}Al_{1.61})O_{10}(OH)_2} +$$

$$+ 1.82\underset{\text{(Ferrihydrite?)}}{FeO(OH)\cdot xH_2O} + 0.42Mg^{2+} + 0.26Si^{4+} + 0.29Al^{3+} + (3-1.82x)H_2O.$$

During the transformation, excess Fe forms possibly ferrihydrite around vermiculite, which is perfectly consistent with the SEM observation. K and Ti, required to form vermiculite, may be released from mica and anatase of the quartz-chlorite schist, respectively. Excess of Mg, Si, and Al may be consumed in the formation of kaolinite and possibly smectite. Additional Fe, Mg, Si, and Al are released during the decomposition of vermiculite, and these may be used again for the formation of ferrihydrite, kaolinite, and smectite. The layered texture of altered chlorite and the similar crystal structures of chlorite and vermiculite[3] suggest that the formation of vermiculite from chlorite may be explained by cation diffusion. However, we have not found any evidence in the SEM images of textural relationships between kaolinite and chlorite or vermiculite and there is a difference in crystal structure between them. This suggests that the formation of kaolinite may be by dissolution and reprecipitation.

It is possible, on the basis of the XRD intensities to qualitatively estimate the abundances of the minerals as a function of depth. Figure 1 schematically compares the uranium concentrations and mineral abundances in drill hole DDH3. The amount of chlorite, which is not altered even at 111 feet (25.9 m deep from the surface vertically), rapidly decreases between 107 and 103 feet (25 and 24 m deep) and chlorite disappears at 103 feet. Vermiculite appears at 107 feet (25 m deep) and is at a maximum at 103 feet (24 m deep) where kaolinite begins to persist. Vermiculite disappears at 86 feet (20 m deep) where kaolinite is predominant as it is in the shallower zone.

The mineral abundances were then compared to the uranium concentrations in ppm[4] along the DDH3 corehole. The comparison indicates that the mineral abundances of chlorite, vermiculite, and kaolinite (smectite) are closely related to the uranium concentrations. The chlorite predominant zone corresponds to the zone of lower U concentrations, the vermiculite predominant zone, to the zone of intermediate U concentrations, and the kaolinite predominant zone, to the zone of highest U concentrations Figure 1). The crystal chemistry of chlorite and its altered minerals may well account for this close relationship.

In any of the minerals, large cations like U cannot be accommodated in the tetrahedral or octahedral sites. Because the chlorite structure has little capacity for large cations in the interlayers, large cations are not accommodated. However, large cations can easily enter the interlayers of vermiculite, hence after the initiation of chlorite alteration U is accommodated in the interlayers. Because ferrihydrite or iron phases, which occur as interstitial materials between vermiculite and chlorite slabs, are adsorbents, it is also possible for U to be adsorbed onto them during the transformation. The kaolinite structure, like that of chlorite, only allows a very limited number of large cations to enter. Therefore, in the kaolinite zone, U is associated with iron phases, ferrihydrite, geothite, and hematite which are formed with the decomposition of vermiculite and the transformation of chlorite to vermiculite. Smectite has a large space for large cations[3]. However, the amount of smectite is small and its role in the accommodation of U remains unknown.

This is illustrated in Fig. 2 where the crystal structures of kaolinite, vermiculite, smectite, and chlorite projected on the (101)

plane (modified from Bailey[3] are compared. In the kaolinite structure, there are no interlayers where larger cations such as pottasium, uranium can be accommodated. Although the chlorite structure has interlayers, they are occupied with (Mg, Fe, Al) octahedral layers, which leaves little space for large cations. On the other hand, the interlayers of smectite and vermiculite have much greater flexibility; exchangeable cations such as K, Mg are more loosely bound to water molecules. The interlayers of smectite and vermiculite can therefore be possible crystallographic sites for uranium.

References

1) Isobe, H., Murakami, T.: Alteration of chlorite in the Koongara uranium deposit and its implication for uranium migration, submitted to Radiochim. Acta.

2) Gray, D.J., Davey, B.G.: Interstratified minerals formed during weathering of chlorite at the Alligator Rivers uranium province Northern Territory. Submitted to Australian Journal of Soil Research.

3) Baily, S.W.: Structures of layer silicates. in: Crystal Structures of Clay Minerals and Their X-ray Identification (G.W. Brindley and G. Brown eds.) Mineralogical Society, London 1980.

4) Ohnuki, T., Murakami, T., Sekine, K., Yanase, N., Isobe, H., Kobayashi, Y.: Migration behavior of uranium and thorium series nuclides in altered quartz-chlorite schist. Submitted to Scientific Basis for Nuclear Waste Management XIII (V.M. Oversby and P.W. Brown eds.) Materials Research Society, Pittsburgh, PA, USA.

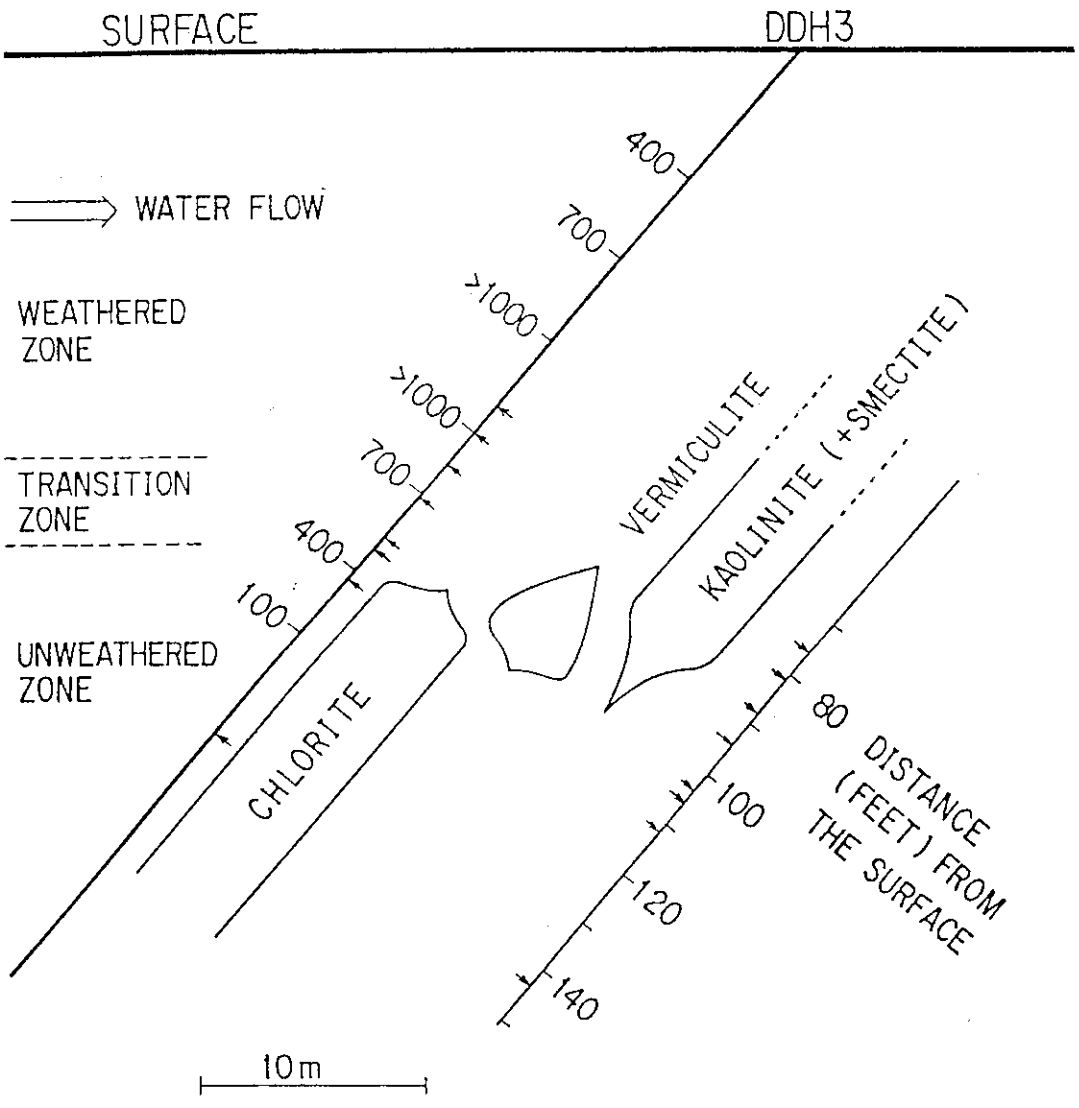

Fig. 1 Comparison of U concentrations ($\mu g\ g^{-1}$) and mineral abundances in DDH3. The arrows indicate the sampling locations for the XRD measurements.

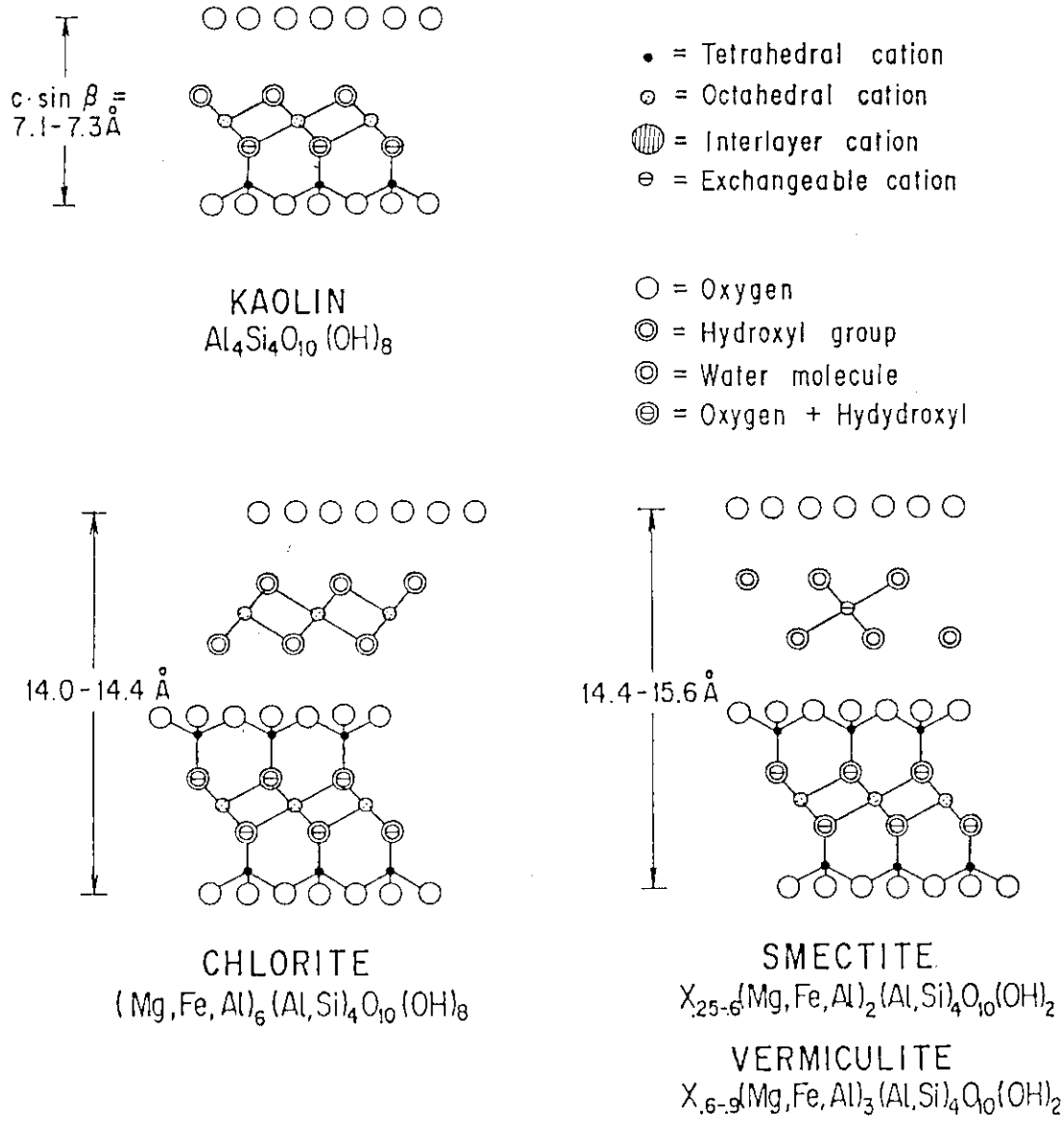

Fig. 2 Comparison of the crystal structures of kaolinite, vermiculite, smectite, and chlorite projected on the (101) plane (modified from Bailey[3]).

3.2 Uranium distribution in mineral phases of rock by a five phase sequential extraction procedure

N. Yanase

Introduction

Selective extraction procedures which had been adopted first to extract traces of metals in specific phases of soil or sediment[1,2,3], were applied to the disequilibrium study of uranium series radionuclides in the rock. The geology, geochemistry and mineralogy of the Koongarra uranium deposit have been investigated and reviewed in a recent report[4]. The ore body consists of a primary ore body and a secondary ore body formed by the leaching of uranium from the primary ore body and its subsequent deposition; the host rock is quartz chlorite schist (Fig. 1). The migration of radionuclides through the Koongarra ore body has been studied as an analogue of radioactive waste repositories. In order to clarify migration mechanisms, it is valuable to identify the significant mineral phase in which isotope disequilibrium has occurred. Nightingale earlier investigated the disequilibrium of ^{238}U, ^{234}U and ^{230}Th in drillcore samples[5]. In this study the sequential extraction procedure used by Nightingale was slightly modified and applied to the rock samples to obtain information on the distribution of uranium in the rock at Koongarra. On the basis of the distribution of uranium, the significant mineral phase of the rock was determined.

Experimental

The analysis of nine rock samples, collected mainly from diamond drill holes in the Koongarra 6109 mN cross section (Fig. 1) is reported here. One gram of crushed material was sequentially treated by the following extraction solutions and the residual mineral and liquid phases were separated by centrifugation and filtration using a 0.45 μm Millipore filter.

The probable minerals dissolved and the extraction reagents used in this study are as follows.

1) Adsorbed trace materials and carbonate minerals by Morgan's solution[2,5].
2) Ferrihydrate, amorphous minerals of Fe, Al and Si, and secondary U minerals by Tamm's solution[1,5].

3) Crystalline iron minerals by CDB solution[3,5].
4) Clay and some refractory minerals by 6 M HCl[5].
5) All remaining resistant minerals by fusion[5].

The uranium and thorium extracted from each mineral phase, was separated by an anion exchange resin (AGX 1×8, 100-200 mesh) after adding the ^{232}U tracer. For the uranium fraction, iron was removed by a di-isopropylether extraction. The uranium was electroplated and measured by alpha spectrometry using a silicon surface barrier detector.

Results and discussion

1) Extraction Procedure

The uranium concentrations and the major mainerals found in the rock samples are listed in Table 1. It can be seen that quartz, mica, clay minerals such as kaolinite, iron minerals (pyrite, hematite, limonite and chalcopyrite) and uranium minerals (pitchblende, autunite and torbernite) are the major minerals in the rock samples. Consequently Nightingale[5] used a sequential extraction procedure for amorphous iron, crystalline iron, residual crystalline, clay and the remaining resistant maineral phases. However, in this study the extraction of uranium by Morgan's solution was added so that we could determine the uranium fraction in the adsorbed or associated carbonate mineral phases, which are more accessible to the groundwater than the amorphous iron mineral phase. On the other hand, the extraction of uranium in the residual crystalline mineral phase was omitted because the amount of uranium in the residual crystalline mineral phase was very small and the $^{243}U/^{238}U$ activity ratio was always similar to that of the crystalline iron mineral phase.

Duplicate analyses were carried out to check the reproducibility of the sequential extraction procedure using the sample DDH1, 4.7 m. The results showed fairly good reproducibility.

2) Uranium Distribution

Figure 2 shows the distribution of uranium in the mineral phases of the rock samples. In the secondary ore body, most of the uranium was contained in the CDB fraction (42-60 %) of all the rock samples, because the iron minerals such as limonite and pyrite are contained in these rock samples and an iron mineral usually incorporate with the uranium in the secondary ore body.

On the other hand, in the primary ore body, 72 % of the total uranium was incorporated with the Tamm's solution extractable minerals in the 19.4-20.5 m region of the drill hole DDH1. This rock sample contains the hematitic mica schist and the uranyl phosphate such as autunite and torbernite. The large amount of uranium in the Tamm's fraction seems to result from the dissolution of uranyl phosphate such as autunite and torbernite.

In the deeper, 33.0-34.3 m, region of the drill hole DDH2, 70 % of the total uranium was extractable with 6 M HCl which mainly dissolves the uranium in the clay mineral phase. However, at the present time we have no evidence for clay mineral existences in this region. As this rock sample contains pitchblende, its insolubility in CDB solution and solubility in 6 M HCl needs to be investigated.

3) $^{234}U/^{238}U$ Activity Ratio

The $^{234}U/^{238}U$ activity ratios of mineral phases of rock samples are shown in Fig. 3. In the secondary ore body, the $^{234}U/^{238}U$ activity ratios of the fusion fraction are greater than unity (2.8-6.3). The mechanism proposed to explain these results suggested that the high enrichment of ^{234}U relative to ^{238}U occurs when ^{234}U recoils into the uranium-poor phase from the adjacent uranium-rich phase and the former phase is isolated from the leaching solution (e.g. groundwater) which causes a preferential leaching of ^{234}U. Therefore the quartz mineral phase in the rock at Koongarra seems to be surrounded by the uranium-rich mineral phase and isolated from the groundwater.

It can be seen from the data that the $^{234}U/^{238}U$ activity ratios for the Morgan's and Tamm's extractions are similar and significantly below unity for all the samples (0.59-0.79 and 0.61-0.78 respectively) in the secondary ore body, and these values are consistent with $^{234}U/^{238}U$ activity ratios for groundwater in this zone. The results support Nightingale's interpretation[5], that is, leaching of uranium and preferential leaching of ^{238}U relative to the ^{234}U in the rock up-gradient, and deposition of uranium in the rock down-gradient are occurring.

In the primary ore body, the $^{234}U/^{238}U$ activity ratio of the fusion fraction was higher than unity in the 19.4-20.5 m region of the drill hole DDH1, a similar result to that obtained in the secondary ore body. However, recoil enrichment of ^{234}U in the fusion fraction appears

not to have occurred in the 33.0-34.3 m region of the drill hole DDH2, where the $^{234}U/^{238}U$ activity ratio in the fusion fraction was unity. There is a possibility that the quartz mineral phase in the deeper region is not surrounded by the uranium-rich mineral phase.

Conclusion

The distribution of uranium, as determined by sequential extraction, can be explained on the basis of the mineral composition of the rock.

In the secondary ore body, the CDB extractable minerals (crystalline iron minerals such as limonite and pyrite) are the significant mineral phase associated with uranium accumulation. The Morgan's and Tamm's solution extractable minerals (adsorbed and carbonate, and amorphous iron minerals respectively) are accessible to groundwater and so their $^{234}U/^{238}U$ activity ratios, less than unity, are equal to that of the groundwater. The remaining resistant minerals (mainly quartz) are the significant mineral phase found to be enriched with ^{234}U by the alpha recoil effect.

However, in the shallow region of the primary ore body, the Tamm's solution extractable minerals (secondary uranium minerals such as autunite and torbernite - uranyl phosphates) are the significant mineral phase associated with the uranium accumulation. In the deeper region of the primary ore body, the 6 M HCl extractable minerals are significant. The relationship between the extraction solutions and the mineral phases has not yet been precisely identified; the mineral phases dissolved by the sequential extraction procedure should be examined by the X-ray diffraction analysis using rock samples from Koongarra.

References

1) Tamm, O.: Uber die Oxalatmethode in der Chemischen Bodenanalyse. Fram Statens Skogsforsoeksans, Stockholm, 27,1(1982).
2) Morgan, M.F.: The Universal Soil Testing System. Connecticut Agricultural Experiment Station Bulletin 372(1935).
3) Mehra, O.P. and Jackson, M.L.: Iron Oxide Removal from Soils and Clays by a Dithionite-Citrate System buffered with Sodium-Bi-Carbonate.

4) Mehra, O.P. and Jackson, M.L.: Iron Oxide Removal from Soils and Clays by a Dithionite-Citrate System buffered with Sodium-Bi-Carbonate. 7th Nat. Conf., Clays Clay Miner., Monograph No.5, p.317 (1960).

4) Snelling, A.A., Koongarra Uranium Deposits, From: 'The Geology of the Mineral Deposits of Australia and Papua New Guinea', F.E. Hughes (ed.), The Australasian Institute of Mining and Metallurgy, Melbourne, Monography 14, 1989 (in press).

5) Nightingale, T.: Distribution of Uranium Series Nuclides throughout the Koongarra Deposit. NUREG/CR-5040 (AAEC/C55, Australian Nuclear Science and Technology Organisation, Lucas Heights NSW 2232, Australia (1987), pp.41-64.

Table 1 Uranium concentrations and the major minerals in the rock samples analyzed by the sequential extraction procedure.

Drill hole	Depth (m)	Concentration of U (ppm)	Major minerals contained*
DDH1	4.7	2271(2.2)	Quartz and limonite stained kaolinitic mica schist.
	19.4-20.5	82300(2.4)	Hematitic mica schist, autunite, quartzite, gumnite and torbernite.
DDH2	33.0-34.3	82500	Pitchblende with hematite gangue in altered schist and quartz gangue replacing altered schist.
DDH3	10.5-11.7	769(3.3)	Limonite, kaolinitic weathered mica schist.
	16.3-17.5	965(2.1)	Carbonaceous pyritic quartz muscovite schist and chalcopyrite.
DDH4	14.0-15.2	536(2.4)	Clayey weathered quartz mica schist.
DDH54	13.5-15.0	963(2.3)	Limonitic, kaolinitic weathered mica schist.
PH55	18.3-19.8	316(2.2)	No data.
PH56	13.5-15.0	323(2.5)	No data.

The figures in parenthesis denote counting error(%).

*:The data on the major minerals contained in the samples is from the Koongarra geological log of Denison Australia Pty Ltd.

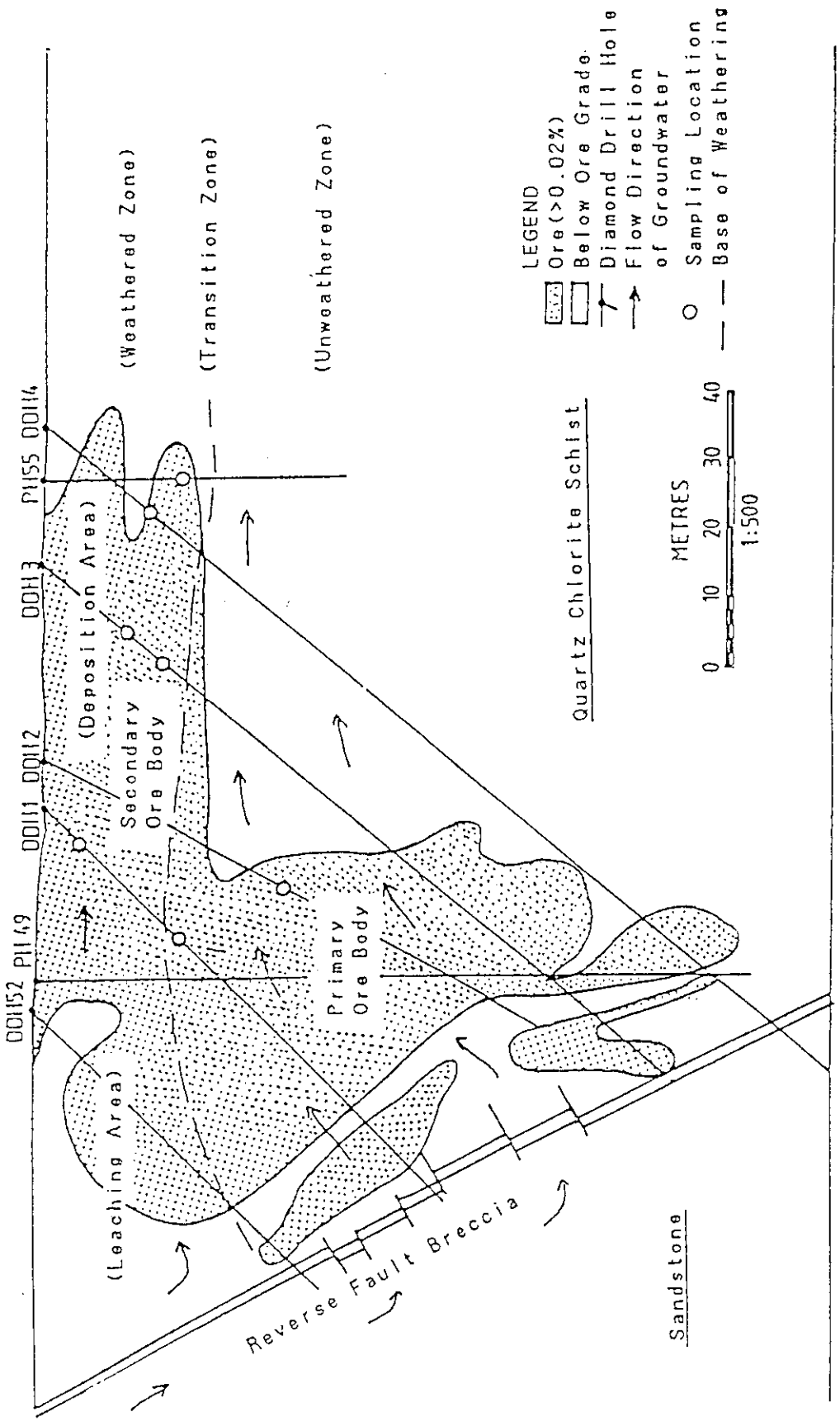

Fig. 1 6109N geological section through the Koongarra uranium ore body and the location of the drillholes.

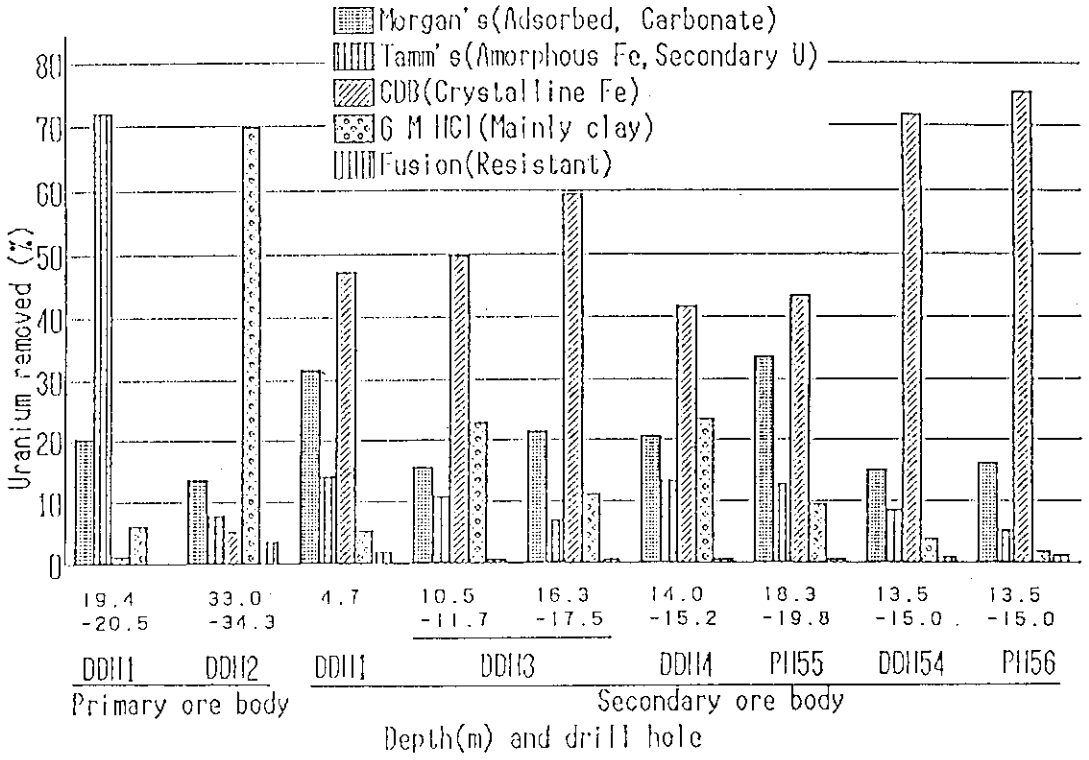

Fig. 2 Distributions of uranium in mineral phases of rock by the five-stage soquential oxtraclion procedure.

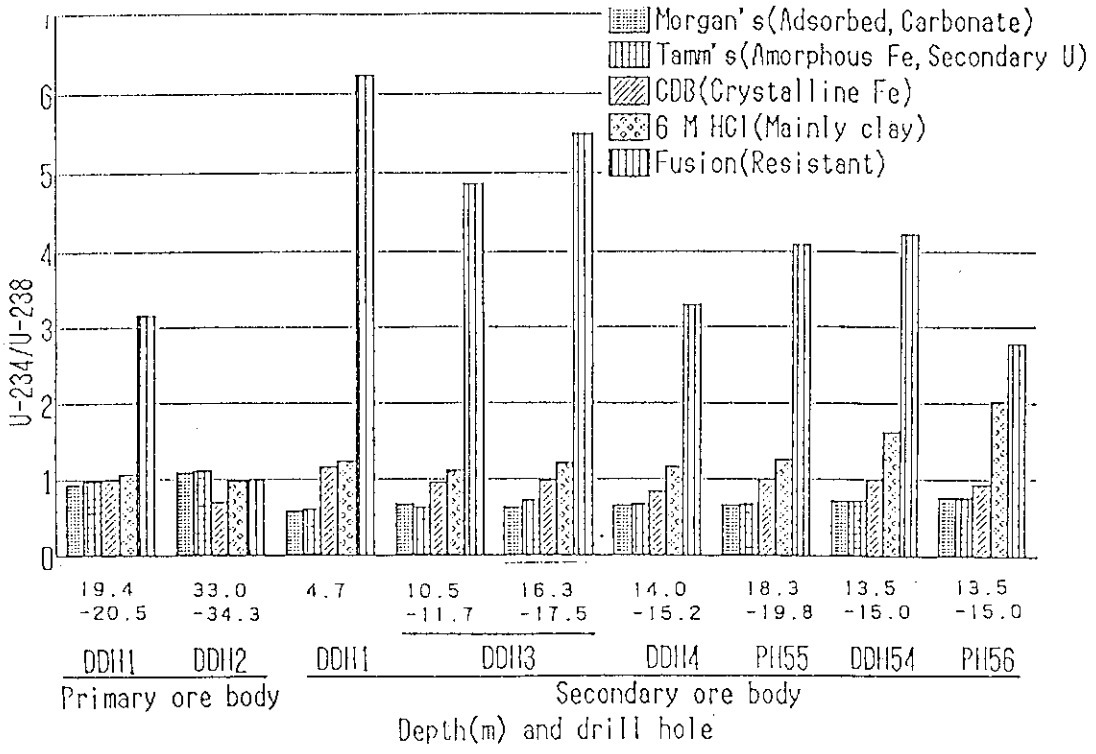

Fig. 3 Variations of $^{234}U/^{238}U$ activity ratios in mineral phases of rock by the five-stage sequential extraction procedure.